



# 1 The High Latitude sNowfall Detection and Estimation aLgorithm 2 for ATMS (HANDEL-ATMS): a new algorithm for the snowfall 3 retrieval at high latitudes

4 Andrea Camplani<sup>1</sup>, Daniele Casella<sup>1</sup>, Paolo Sanò<sup>1</sup>, Giulia Panegrossi<sup>1</sup>

5 <sup>1</sup>National Research Council of Italy, Institute of Atmospheric Sciences and Climate (CNR-ISAC), Via del Fosso  
6 del Cavaliere 100, 00133 Rome, Italy

7 *Correspondence to:* Andrea Camplani (Andrea.Camplani@artov.isac.cnr.it)

8 **Abstract.** Snowfall detection and quantification are challenging tasks in the Earth system science field. Ground-  
9 based instruments have limited spatial coverage and are scarce or absent at high latitudes. Therefore, the  
10 development of satellite-based snowfall retrieval methods is necessary for the global monitoring of snowfall.  
11 Passive Microwave (PMW) sensors can be exploited for snowfall quantification purposes because their  
12 measurements in the high-frequency channels (> 80 GHz) respond to snowfall microphysics. However, the highly  
13 non-linear PMW multichannel response to snowfall, the weakness of snowfall signature and the contamination by  
14 the background surface emission/scattering signal make snowfall retrieval very difficult. This phenomenon is  
15 particularly evident at high latitudes, where light snowfall events in extremely cold and dry environmental  
16 conditions are predominant. ML techniques have been demonstrated to be very suitable to handle the complex  
17 PMW multichannel relationship to snowfall. Operational microwave sounders on near-polar orbit satellites such  
18 as the Advanced Technology Microwave Sounder (ATMS), and the European MetOp-SG Microwave Sounder in  
19 the future, offer a very good coverage at high latitudes. Moreover, their wide range of channel frequencies (from  
20 23 GHz to 190 GHz), allows for the radiometric characterization of the surface at the time of the overpass along  
21 with the exploitation of the high-frequency channels for snowfall retrieval. The paper describes the High Latitude  
22 sNow Detection and Estimation aLgorithm for ATMS (HANDEL-ATMS), a new machine learning-based  
23 snowfall retrieval algorithm developed specifically for high latitude environmental conditions and based on the  
24 ATMS observations.

25 HANDEL-ATMS is based on the use of an observational dataset in the training phase, where each ATMS  
26 multichannel observation is associated with coincident (in time and space) CloudSat Cloud Profiling Radar (CPR)  
27 vertical snow profile and surface snowfall rate. The main novelty of the approach is the radiometric  
28 characterization of the background surface (including snow covered land and sea ice) at the time of the overpass  
29 to derive multi-channel surface emissivities and clear-sky contribution to be used in the snowfall retrieval process.  
30 The snowfall retrieval is based on four different artificial neural networks for snow water path (SWP) and surface  
31 snowfall rate (SSR) detection and retrieval. HANDEL-ATMS shows very good detection capabilities - POD =  
32 0.83, FAR = 0.18, and HSS = 0.68 for the SSR detection module. Estimation error statistics show a good  
33 agreement with CPR snowfall products for  $SSR > 10^{-2} \text{ mm h}^{-1}$  (RMSE  $0.08 \text{ mm h}^{-1}$ , bias= $0.02 \text{ mm h}^{-1}$ ). The  
34 analysis of the results for an independent CPR dataset and of selected snowfall events evidence the unique  
35 capability of HANDEL-ATMS to detect and estimate SWP and SSR also in presence of extreme cold and dry  
36 environmental conditions typical of high latitudes.

## 37 1 Introduction

38 Snowfall retrieval is one important topic in the atmospheric science field. On a global scale, snowfall represents  
39 only 5 % of the total global precipitation but it is predominant above  $60\text{-}70^\circ \text{ N/S}$  (see *Levizzani et al., 2011*). In  
40 recent years, several studies have highlighted the strong influence of global warming on snowfall distribution and  
41 regimes, especially at high latitudes (see *Liu et al., 2009, Liu et al., 2012, Bintanja & Selten, 2014, Vihma et al.,*  
42 *2015*). However, global snowfall quantification is a challenging topic in weather sciences. Ground-based  
43 instruments such as raingauges or snowgauges provide only punctual measurements which can not fully capture  
44 the spatial variability of precipitation phenomena; moreover, the variability of snowflake shape and density has a  
45 strong influence on their fall speed and trajectories and therefore gauge-based measurements of falling snow result  
46 to be less accurate than for rain (see *Skofronick-Jackson et al., 2015*). Weather radars can provide areal  
47 measurements of precipitation - the rate estimation is based on the conversion of the measured backscattered  
48 radiation to precipitating hydrometeors content - but such operation presents some technical limitations (see *Kidd*



49 & Huffman, 2011). Finally, most of the regions where snowfall is predominant - such as Greenland, Siberia,  
50 Canada, and Antarctica - are uninhabited or otherwise sparsely populated areas where weather observation  
51 networks are very scarce or totally absent. Therefore, the development of satellite-based methods for snowfall  
52 retrieval is necessary for global monitoring of snowfall. Passive Microwave (PMW) sensors on board polar  
53 orbiting satellites can be exploited for snowfall detection purposes because the microwave (MW) signal is directly  
54 responsive to the spatial distribution and microphysics properties of precipitation-sized hydrometeors in the  
55 clouds; at the same time, the use of PMW sensors guarantees a high spatial coverage and high temporal resolution  
56 (see Kidd & Huffman, 2011).

57 PMW snowfall detection and quantification is typically based on the ability to interpret the snowfall scattering  
58 signature in the high frequency channels ( $> 90$  GHz), which respond more effectively to ice microphysics and are  
59 less prone to surface effects than low frequency channels, and to distinguish it from the clear-sky (surface and  
60 atmosphere) contribution (e.g., Panegrossi *et al.*, 2017). However, several factors make the PMW snowfall signal  
61 ambiguous and the relationship between multichannel measurements and surface snowfall intensity highly non-  
62 linear, especially in extremely cold/dry environmental conditions (see Panegrossi *et al.*, 2022). The snowfall  
63 scattering signal is relatively weak and is highly dependent on the complex microphysical properties of snowflakes  
64 (Kim *et al.*, 2008, Kulie *et al.*, 2010, Kongoli *et al.*, 2015), it is often masked by supercooled liquid water emission  
65 signal, and can be contaminated by the extremely variable background surface emissivity (Liu and Seo, 2013,  
66 Takbiri *et al.*, 2019, Rahimi *et al.*, 2017), especially in cold and dry conditions typical of the high latitude regions  
67 (Camplani *et al.*, 2021). In this context, the availability of the last generation microwave radiometers - such as the  
68 conically-scanning radiometer GPM Microwave Imager (GMI) and the cross-track scanning radiometer Advanced  
69 Technology Microwave Sensor (ATMS) - whose channels cover a wide range of frequencies - offers new  
70 possibilities for global snowfall monitoring. The multi-channel PMW observations can be used for both a  
71 radiometric characterization of the background surface - using the low-frequency channels ( $< 90$  GHz) - and for  
72 the detection and the estimation of the snowfall using the high-frequency channels ( $> 90$  GHz) (see Panegrossi *et al.*  
73 *et al.*, 2022).

74 The PMW capability to characterize physically and radiometrically the background surface varies from sea to  
75 land, especially for the identification of cold/frozen surfaces. For what concerns the ocean, sea ice detection using  
76 PMW observations has been a well-documented topic in the remote sensing science field since the 70s. This is  
77 due to the strong contrast between sea ice ( $\approx 0.9$ ) and open water ( $\approx 0.5$ ) emissivity values at the MW low-  
78 frequency range ( $\sim 19$  GHz) (see Comiso, 1983). Other studies highlighted the ability to discriminate between  
79 different types of ice using a set of low-frequency window channels, because the differences between the  
80 emissivities of the different types of sea ice increase with increasing frequency; in particular, at higher frequencies  
81 (30-50 GHz) the contrast between the emissivity of “new” ice and “old” ice increases, with a decrease of the  
82 emissivity at higher frequencies for “older” sea ice (see Comiso, 1983, Ulaby *et al.*, 2014). Moreover, it has been  
83 observed that the simultaneous presence of open water and sea ice causes a decrease in the low-frequency channel  
84 emissivity; the observed emissivity can be considered as a linear combination of the emissivity spectra of sea ice  
85 and open water (see Ulaby *et al.*, 2014). For what concerns continental areas, the detection of snow-covered land  
86 surfaces using MW results to be more difficult. In dry conditions, a snowpack acts as a volume scatterer; the  
87 scattering effect is dependent on the grain size and shape and on the depth of the snowpack (see Clifford, 2010).  
88 However, the presence of liquid water can mask the scattering signature (see Mätzler & Hüppi, 1989). At the same  
89 time, large areas of Greenland and Antarctica could appear as “scatter-free”, although these areas throughout the  
90 year are covered by dry snowpacks. Finally, some snow-free areas, such as rocky mountains and cold deserts,  
91 present a scattering signature very similar to that of the snowpack (see Grody & Basist, 1996). Therefore, the  
92 detection of snow-covered areas is very complex. A set of several tests, each of which identifies snowpacks  
93 characterized by different physical and radiometric characteristics, may be used.

94 This paper describes the development of a machine learning-based algorithm for snowfall retrieval (the High  
95 Latitude sNowfall Detection and Estimation aLgorithm for ATMS, HANDEL-ATMS), exploiting ATMS  
96 radiometer multi-channel measurements and using the CloudSat Cloud Profiling Radar (CPR) snowfall products  
97 as reference. The algorithm has been developed focusing on the typical conditions of high latitude regions - low  
98 humidity, low temperature, presence of snowpack on land or sea ice over ocean, and light snowfall intensity.

99 The main novelty of the approach is the exploitation of the ATMS wide range of channels (from 22 GHz to 183  
100 GHz) to obtain the radiometric characterization of the background surface at the time of the overpass. The derived



101 surface emissivities are used to infer the clear-sky contribution to the measured TBs in the high-frequency  
102 channels in the snowfall retrieval process. Moreover, the algorithm is based on the exploitation of an observational  
103 dataset where each ATMS multichannel observation is associated with coincident (in time and space) CloudSat  
104 CPR vertical snow profile and surface snowfall rate (hereafter ATMS-CPR coincidence dataset).  
105 Several snowfall retrieval algorithms for cross-track scanning radiometers have evolved in the last 20 years  
106 starting from the Advanced Microwave Sounder Unit-B (AMSU-B) (Kongoli et al., 2003, Skofronick-Jackson et  
107 al., 2004, Noh et al., 2009, Liu and Seo 2013), and Microwave Humidity Sounder (MHS) (see Liu & Seo, 2013,  
108 Edel et al., 2020), and evolving to ATMS (Kongoli et al., 2015, Meng et al., 2017, Kongoli et al., 2018, You et al.,  
109 2022, Sanò et al., 2022). Some of them are based on radiative transfer simulations of observed snowfall events  
110 (Kongoli et al., 2003, Skofronick-Jackson et al., 2004, Kim et al., 2008), or on in-situ data (see Kongoli et al., 2015,  
111 Meng et al., 2017, Kongoli et al., 2018), others on CPR observations (Edel et al., 2020, You et al., 2022, Sanò et al.,  
112 2022), or a combination of them (Noh et al., 2009, Liu & Seo, 2013). In the last five years, there has been an  
113 increasing use of machine learning (ML) approaches trained on CPR-based coincidence datasets. These  
114 approaches have proven to be very effective for snowfall retrieval. On one side, ML techniques are suitable to  
115 handle the complex, nonlinear PMW multichannel response to snowfall (e.g., Rysman et al., 2018, Edel et al.,  
116 2020, Sanò et al. 2022). On the other side, the use of CPR-based datasets overcomes some of the limitations  
117 deriving from the assumptions to be made in cloud-radiation model simulations (e. g., the microphysics scheme,  
118 the emissivity of the background surface, scattering properties of ice hydrometeors), which are particularly  
119 problematic for snowfall estimation. However, some limitations of the radar product used as reference and issues  
120 related to the spatial and temporal matching between the CPR and the PMW radiometer measurements introduces  
121 some uncertainty.

122 For what concerns ATMS, the ML-based Snow retrieval ALgorithm fOr gpM–Cross Track (SLALOM-CT)  
123 (Sanò et al., 2022) has been developed within the EUMETSAT Satellite Application Facility for Hydrology (H  
124 SAF) in preparation for the launch of the EPS-SG Microwave Sounder (MWS). Similarly to HANDEL-ATMS, it  
125 is trained on a ATMS-CPR coincidence dataset. SLALOM-CT is the evolution for cross-track scanning  
126 radiometers of the Snow retrieval ALgorithm fOr GMI (SLALOM) (Rysman et al., 2018, Rysman et al., 2019)  
127 which was the first ML algorithm for snowfall detection and retrieval for GMI trained and tested on GMI-CPR  
128 coincident observations made available in the NASA GPM-CloudSat coincidence dataset (Turk et al., 2021a).  
129 One of the novelties in the SLALOM (SLALOM-CT) approach is the use of the GMI (ATMS) low-frequency  
130 channels to better constrain the snowfall retrieval to the characteristics of the surface at the time of the overpass  
131 (Turk et al., 2021b). SLALOM-CT is based on a modular scheme, i.e., four separate modules are used for snowfall  
132 detection, supercooled water layer detection, snow water path (SWP) and surface snowfall rate (SSR) estimate.  
133 The predictor set is composed of the ATMS TBs and some environmental variables ( $T_{2m}$ , TPW, and principal  
134 components derived from temperature and humidity profiles).

135 However, none of the algorithms mentioned here were trained specifically for the extreme conditions typical of  
136 high latitudes. The present work has the aim to develop an algorithm for snowfall detection and estimation by  
137 exploiting the large frequency range typical of the last generation radiometers and to obtain a radiometric  
138 characterization of the background surface at the time of the satellite overpass in order to highlight the complex  
139 relationship between upwelling radiation and snowfall signature, which makes the detection very difficult in the  
140 typical conditions of the high latitudes.

141 This article is organized as follows: Section 2 provides background information on ATMS and CPR, on the  
142 methodology used to build the coincidence dataset and on the machine learning approaches used to develop the  
143 algorithm. In Section 3 the algorithm structure is described. In Section 4 the overall performance scores are  
144 reported and analyzed; a case study is analyzed and a comparison with SLALOM-CT is reported. Section 5 is  
145 dedicated to the summary of the main results and to the conclusions.

## 146 2. Instruments and methods

### 147 2.1 Advanced Technology Microwave Sounder (ATMS)

148 ATMS is a total power cross-track scanning radiometer within  $52.7^\circ$  off the nadir direction. It has a total of 22  
149 channels with the first 16 channels primarily used for temperature sounding from the surface to about 1 hPa (45  
150 km) and the remaining channels used for water vapor sounding in the troposphere from the surface to about 200  
151 hPa (10 km). There are two receiving antennas: one serving channels 1–15 below 60 GHz, and the other for  
152 channels above 60 GHz. The beamwidth changes with frequency and is  $5.2^\circ$  for channels 1–2 (23.8–31.4 GHz),



153 2.2° for channels 3–16 (50.3–57.29 and 88.2 GHz), and 1.1° for channels 17–22 (165.5–183.3 GHz). The  
154 corresponding nadir resolutions are 74.78, 31.64, and 15.82 km, respectively. The outmost field of view (FOV)  
155 sizes are 323.1 km × 141.8 km (cross-track × along-track), 136.7 km × 60.0 km, and 68.4 km × 30.0 km,  
156 respectively. The ATMS can be considered the evolution of the three main previous cross-track scanning  
157 radiometers: Advanced Microwave Sounding Unit-A (AMSU-A), Advanced Microwave Sounding Unit-B  
158 (AMSU-B), and Microwave Humidity Sounder (MHS). Seventeen ATMS channels (channels 1–3, 5–15, 17, 20,  
159 and 22) have the same frequencies as its two predecessors AMSU, two ATMS channels (channels 16 and 18) have  
160 slightly different frequencies from AMSU channels, and three new channels (channels 4, 19 and 21) have been  
161 added to ATMS (see *Weng et al, 2012*). ATMS is currently carried by three near-polar orbiting satellites, Suomi  
162 National Polar-orbiting Partnership (SNPP) NOAA-20, and NOAA-21 providing global coverage including polar  
163 regions. Moreover, each satellite revisiting time is equal to 12 hours at the equator, but drops to 100 minutes over  
164 the polar regions, ensuring a very high temporal resolution for the research area of interest in this work. Moreover,  
165 the operational nature of the mission guarantees observations for the next decades. It is worth noticing that the  
166 polarization of ATMS channels is not defined as vertical or horizontal, but as “Quasi-Vertical” or “Quasi-  
167 Horizontal”. The “Quasi” prefix is used to indicate that ATMS (and any other cross-track scanner) measures  
168 vertical or horizontal polarization only when looking at nadir and a mixture of V and H polarization for off-nadir  
169 scan angles.

## 170 2.2 Cloud Profiling Radar (CPR)

171 The CPR is a 94 GHz nadir-looking radar onboard CloudSat. CloudSat was launched on April 28, 2006; the W-  
172 band (94 GHz) Cloud Profiling Radar (CPR) operations began on June 2, 2006. CPR has been acquiring the first-  
173 ever continuous global time series of vertical cloud structures and vertical profiles of cloud liquid and ice water  
174 content with a 485-m vertical resolution and a 1.4-km antenna 3-dB footprint. The reference CloudSat snowfall  
175 product is the 2C-Snow-Profile (2CSP) product (Version 5 is used in this work). It provides estimates of snowfall  
176 characteristics for each observed profile. In particular, it provides an estimate of the Snow Water Path (SWP), i.  
177 e., the total snow water content integrated over the atmospheric column, and of the Surface Snowfall Rate (SSR)  
178 (see *Stephens et al, 2008*). SWP is estimated also when there is no snowfall at the ground level; therefore, the  
179 presence of SWP is not always linked to the presence of SSR, especially in warmer near-surface conditions (see  
180 *Wood & L'Ecuyer, 2018*). 2CSP has several limitations, such as the contamination of the signal in the lowest 1000  
181 - 1500 m of the profile due to ground-clutter, the underestimation of the heavy snowfall events, due to attenuation  
182 of the radar signal in these conditions, and the limited temporal sampling (although it is higher in the polar  
183 regions), and the day-only operation mode since 2011, which limits its use during the winter seasons (see *Milani*  
184 *and Wood, 2021, Panegrossi et al, 2022*). However, 2CSP has been demonstrated to be more accurate than GPM  
185 Dual-frequency Precipitation Radar (DPR) snowfall products (see *Casella et al, 2017*) and in good agreement  
186 with estimates obtained by ground-based radars (e.g., *Mroz et al, 2021*), although it is affected by underestimation  
187 for medium-heavy snowfall events. Moreover, the polar orbit and the W-band high sensitivity make CPR suitable  
188 for snowfall monitoring at higher latitudes (as demonstrated in several studies, *Kulie et al, 2016, Milani et al,*  
189 *2018*) typically characterized by light/moderate intensity (*Beranghi et al, 2016*).

## 190 2.3 ATMS-CPR Coincidence Dataset

191 The present study is based on a coincidence dataset between CPR and ATMS observations between January 2014  
192 and August 2016. The same dataset has been used for the development of SLALOM-CT (*Sandò et al, 2022*). Each  
193 coincidence comes from observations from CloudSat CPR and ATMS - onboard SNPP - within a maximum 15-  
194 minute time window. Moreover, the elements in the dataset have been selected by removing all corrupted data  
195 and by applying an additional filter based on the minimum distance between CPR and ATMS IFOV center which  
196 (22 km). The zonal distribution of the coincidences is due to the orbital geometry of CloudSat and SNPP, which  
197 are both sun-synchronous with a relatively small difference in the satellite height (i. e., about 689 km and 833 km  
198 for CloudSat and SNPP respectively). Therefore, the coincidence dataset is built from longer orbit fragments  
199 (often semi-orbits) and by a very large number of elements near the poles. There is an asymmetry in the CPR  
200 sampling between the Northern and the Southern hemisphere that can be observed in the dataset due to the CPR  
201 daytime-only mode operation since 2011, which influences mostly the acquisitions in the Southern Polar region.  
202 The database has been built considering the horizontal resolution of the high-frequency channels of ATMS. The  
203 CPR snowfall product used as reference is the 2CSP (v.5). Some model-derived variables have been added to the  
204 dataset to be used as ancillary variables. Both 2D and 3D environmental variables have been obtained from the



205 European Center Medium Weather Forecast (ECMWF). In particular, they are obtained from the CPR ECMWF-  
206 AUX product where the set of ancillary ECMWF atmospheric state variable data is associated with each CloudSat  
207 CPR bin (the product is described by *Partain, 2022*). Moreover, a cloud-cover fraction index, which indicates the  
208 fraction of CPR observations where cloud is observed on the total CPR observations within each ATMS pixel, is  
209 added to the dataset.

210 Information about the presence of supercooled water is added in the coincidence dataset to be used towards the  
211 correct interpretation of the snowfall signal in presence of supercooled water layers. The supercooled water  
212 information has been extracted from the DARDAR product (see DARDAR). DARDAR, which stands for  
213 raDAR+LiDAR, combines CPR radar and Cloud-Aerosol Lidar with Orthogonal Polarization (CALIOP) lidar  
214 observations, onboard Cloud-Aerosol Lidar and Infrared Pathfinder Satellite Observations (CALIPSO) satellite,  
215 and estimates both the cloud water phase and the ice water content and ice particle effective radius (see *Battaglia*  
216 *& Delanoë, 2013*, *Ceccaldi et al, 2013*). In particular, the coincidence dataset includes an index indicating the  
217 presence of supercooled liquid water within each ATMS pixel, calculated as the fraction of DARDAR  
218 observations where supercooled water within and on the top of the cloud is observed to the total DARDAR  
219 observations within each pixel.

220 The association of ATMS TBs and CPR products has been done by averaging the CPR snow products with a  
221 Gaussian function approximating the ATMS high-frequency antenna pattern (varying with the scan angle). It is  
222 worth noting, however, that the ATMS IFOV is under-sampled by the narrow swath of the CPR (see *Sanò et al.,*  
223 *2022* for details).

#### 224 **2.4 Machine Learning approaches**

225 The algorithm is based on different machine-learning (ML) techniques. These techniques are widely applied in  
226 Earth observation because of their ability to approximate, to an arbitrary degree of accuracy, complex nonlinear,  
227 and imperfectly known functions. A fundamental characteristic of these techniques is that the training process  
228 eliminates the need for a well-defined physical or numerical model that describes the relationships between the  
229 input values and output results, allowing the identification of these relationships during the learning phase (see  
230 *Sanò et al, 2022*). Moreover, clustering techniques have been used to characterize from a radiometric point of  
231 view the background surface. In particular, an unsupervised clustering technique has been used to identify  
232 emissivity clusters with small internal variability, and a supervised clustering technique has been used to identify  
233 an emissivity spectrum based on other parameters.

##### 234 **2.4.1 Artificial Neural Networks**

235 An Artificial Neural Network (ANN) is an information-processing system inspired by the functioning of  
236 biological neural networks. It is composed of neurons, i. e., elements where the information is processed using an  
237 activation function, and the connecting links between the neurons, where a weight multiplies the deriving from  
238 the upstream signal. In particular, the HANDEL-ATMS snowfall detection and estimation modules have been  
239 developed using feedforward multilayer neural network architectures, i. e., a neural network architecture where  
240 the neurons are arranged in layers; each neuron belonging to a layer receives, as input to its transfer function, a  
241 weighted sum of the outputs of the previous layer. This architecture, which is defined by the number of layers,  
242 the number of neurons for each layer, and the transfer function of each neuron, has to be designed beforehand.  
243 The weights of connection links and the bias values for each layer are estimated with a training process, based on  
244 the Levenberg–Marquardt algorithm (see *Sanò et al, 2015*).

##### 245 **2.4.2 Self Organizing Maps**

246 The unsupervised clustering method used for the background surface classification is the Self Organizing Map  
247 (SOM) method (see *Kohonen, 2012*). The characteristic of this method is to assume a topological structure among  
248 the cluster units: the maps can be represented as a neuron network where each neuron represents a cluster. Similar  
249 to the k-means clustering method, the neuron is associated with an input vector by minimizing a distance  
250 measurement; however, not only the weight vector of the winning neuron is updated, but also the weight vectors  
251 of all the neurons which are considered topologically close (see *Faussett, 2006*). Therefore, classes that are close  
252 to each other from a topological point of view can be considered similar also from a physical and radiometric  
253 point of view (see *Munchak et al, 2020*). SOMs have been already used to make a classification of the background  
254 surface by creating clusters based on emissivity values (see *Prigent et al, 2001, Cordisco et al, 2006, Prigent et*  
255 *al, 2008, Munchak et al, 2020*).



#### 256 **2.4.3 Linear Discriminant Analysis**

257 Several supervised clustering methods have been tested in this study, such as the linear discriminant analysis, the  
258 quadratic discriminant analysis, the classification tree, and the nearest neighbor method. The final choice came  
259 down to linear discriminant analysis (LDA) because this method guarantees satisfactory accuracy in the results  
260 with a difference between the performances of the training and the test phase which is not too significant, and a  
261 computational effort which is not too high. Discriminant Analyses are classification methods based on the  
262 assumption that each observation is a realization of a normal distribution - if there is a single predictor - or a  
263 multivariate normal distribution - if it is based on more than one predictor. In particular, LDA assumes that clusters  
264 have a common covariance analysis; therefore, the decision boundary between the clusters results to be linear  
265 relationships (see *Hastie et al, 2009*).

#### 266 **3 Algorithm description**

267 The configuration of the HANDEL-ATMS is summarized in the Flowchart in Figure 1. The process begins with  
268 the classification of the background surface using the PMW Empirical cold Surface Classification Algorithm  
269 (PESCA, *Camplani et al, 2021*); then, the surface emissivity spectra are derived through refinement process based  
270 on LDA and these are used to estimate clear-sky simulated TB ( $TB_{sim}$ ) using the ECMWF-AUX atmospheric  
271 temperature and water vapor profiles. Then, the differences between the  $TB_{sim}$  and the ATMS observed TB ( $TB_{obs}$ )  
272 are evaluated ( $\Delta TB_{obs-sim} = TB_{obs} - TB_{sim}$ ). Four ANNs are then applied to a predictor set consisting of ATMS  
273  $TB_{obs}$ ,  $\Delta TB_{obs-sim}$ , a surface classification flag, and other environmental and ancillary parameters. Finally, the  
274 pixels classified with the presence of snowfall by the detection module, are used in the estimation modules while  
275 for no-snowfall flagged pixels the snowfall rate value is set to 0 mm/h. In the following sections the main blocks  
276 of the algorithm are described in detail.

#### 277 **3.1 Surface Classification and emissivity spectra estimation**

##### 278 **3.1.1 PESCA Design and Performances**

279 The classification and radiometric characterization of the background surface at the time of the satellite overpass  
280 is based on PESCA exploiting ATMS low-frequency channels (*Camplani et al., 2021*). The algorithm  
281 discriminates between frozen and unfrozen surfaces (sea ice and open water, snow-covered land and snow-free  
282 land), and identifies 10 surface classes (4 over ocean, 5 over land, 1 for coast). The algorithm has been tuned  
283 against the NASA AutoSnow product (see *Romanov, 2019*), which gives daily maps of sea ice and snow cover.  
284 For each ATMS observation, a flag reporting the AutoSnow class percentage (sea ice, open water, snow-covered  
285 land, snow-free land) has been calculated; then, a threshold has been applied to discriminate between sea ice and  
286 open water pixels (sea ice AutoSnow class > 10 %) and between snow-covered and snow-free land pixels (snow-  
287 covered land AutoSnow class > 50 %). ATMS pixels have been classified into land, ocean, and coast pixels using  
288 a land-sea mask.

289 The land module discriminates between snow-free land and snow-covered land and identifies four different snow  
290 cover classes (Perennial, Winter Polar, Thin, and Deep Dry). It is based on a decision tree that makes use of a  
291 limited number of inputs (the ratio  $TB_{23QV}/TB_{31QV}$  - **ratio**, the difference between  $TB_{23QV}$  and  $TB_{88QV}$  or Scattering  
292 Index - **SI**, 23 GHz pseudo-emissivity (i. e. the ratio between an observed brightness temperature (TB) and a near-  
293 surface temperature value) - **pem<sub>23</sub>**). The module has been described by *Camplani et al, 2021*.

294 For what concerns the ocean module, a simple relationship to distinguish between sea ice and open water  
295 observations has been identified. In Figure 2 a Cartesian plane where the x-axis represents 23 GHz observed TB  
296 and the y-axis represents the near-surface temperature ( $T_{2m}$ ) is shown. - In the figure each point represents a  
297 pseudo-emissivity value, and the color describes the mean AutoSnow sea ice percentage within each bin (see  
298 Figure 2, left panel). It is possible to observe that open water (0 % of sea ice, blue) and sea ice (100 % of sea ice,  
299 red) are characterized by very different pseudo-emissivities. A transition area between open water and sea ice  
300 pseudo-emissivity values can be observed: these values characterize IFOVs where both open water and sea ice  
301 are present. The simple relationship for sea ice identification is reported in the left panel as a green line where the  
302 condition for sea ice identification is defined by Equation 1.

$$303 \quad TB_{23QV} > T_{2m} - 96 K$$

304 (1)

305 The analysis of the two low-frequency pseudo-emissivity values has been used to obtain information about sea  
306 ice characteristics downstream of the sea ice/open water identification. This is possible because sea ice surface  
307 emissivity for low-frequency channels can be approximated by the pseudo-emissivity, because the interaction



308 between the MW radiation and the atmosphere in the MW low-frequency channels is not significant, especially  
309 in cold and dry conditions. For that reason, the 23 GHz pseudo-emissivity ( $pem_{23}$ ) and the 31 GHz pseudo-  
310 emissivity ( $pem_{31}$ ) have been used. In Figure 3 (top panel) it is possible to observe that there are sea ice classified  
311 observations characterized by the contemporary presence of open water and sea ice above the bisector of the plane  
312 and in correspondence with low emissivity values. In the center panel, where the color represents sea ice  
313 occurrences, it is evident the presence of a cluster, in correspondence with high pseudo-emissivity, with two  
314 “tails”: the one above the bisector, the other below it. This behavior has been used to identify 3 different sea ice  
315 classes (New Sea Ice, Broken Sea Ice, and Multilayer Sea Ice). This algorithm is based on a Nearest Neighbour  
316 Method based on a set of points that define the areas of interest for each sea ice class. In Figure 3 (bottom panel)  
317 a classification representation is reported: the markers represent the points on which the Nearest Neighbor method  
318 is based. The names of the classes have been chosen by analyzing the physical properties of the classes and by  
319 comparing the estimated emissivity spectra with previous works (*Hewison & English, 1999, Munchak et al, 2020*).  
320 PESCA’s upper working limits for  $T_{2m}$  and atmospheric total precipitable water (TPW) have been established to  
321 280 K and 10 mm, respectively (see *Camplani et al, 2021* for details). Moreover, the land module does not work  
322 in the high elevation areas outside the polar regions (surface elevation > 2500 m for latitude < 67 ° N/S) because  
323 the ATMS low spatial resolution does not allow for depicting the small-scale snow-cover variability that  
324 characterizes the orographic regions. Within these well-defined limits, the PESCA manages to optimally  
325 discriminate between sea ice, open water, snow-free land and snow-covered land. An analysis carried out using  
326 the ATMS-CPR coincidence dataset highlights that the presence of cloud cover does not influence the overall  
327 PESCA performances (not shown). The statistical scores (POD, FAR, HSS) of PESCA identification of sea ice  
328 and snow cover (using AutoSnow as reference) are summarized in Table 1. In the defined environmental  
329 conditions PESCA manages to optimally detect the presence of a frozen background (sea ice over the ocean, snow  
330 covered land over the continental part) at the time of the satellite overpass. It is important to underline that the  
331 difference between the HSS values is due to the different number of correct negative observations, which has a  
332 strong influence on HSS values.

333 An analysis of the physical characteristics of the PESCA classes has been conducted by considering the mean  $T_{2m}$ ,  
334 the geographical and seasonal distribution associated with each class. For what concerns land class characteristics  
335 and properties, refer to *Camplani et al., 2021*. For what concerns sea ice, the New Sea Ice class, which is detected  
336 during the winter, at high latitudes, and for low temperatures represents the sea ice that forms during the winter.  
337 The Broken Sea Ice class, which is predominant in the lower latitudes and whose occurrence increases during the  
338 spring, represents the co-presence of sea ice and water typical of the intermediate seasons and in presence of  
339 melting phenomena. The Multilayer Sea Ice class, which is detected only at high latitudes, for very low  
340 temperatures, and with a constant occurrence during the year, represents the ice typical of those regions where  
341 extremely cold conditions allow its presence during the whole year.

### 342 3.1.2 PESCA emissivity spectra estimation

343 The emissivity spectra of each class have been estimated by applying the PESCA algorithm to the cloud-free (0%  
344 CPR cloud mask fraction, i.e., clear sky) ATMS observations in the ATMS-CPR dataset satisfying PESCA  
345 working limits. The ATMS clear-sky TBs measured for each PESCA surface class have been used as input to an  
346 inverse radiative transfer model. The emissivity spectra have been estimated by calculating the mean and the  
347 standard deviation of the emissivity values for each class (excluding the values lower than the 10th percentile and  
348 higher than the 90th percentile). The emissivity spectra dependence on the ATMS viewing angle for polarized  
349 surfaces has been neglected because an analysis of such dependence in the ATMS-CPR coincidence dataset has  
350 shown that it is significant only for larger viewing angles (tot for >40 °). This is due to the fact that cross-track  
351 scanning radiometers measure a signal (off-nadir) which derives from a mixture between the two polarizations  
352 (e.g., quasi-vertical, QV, and quasi-horizontal, QH). As a consequence, although the emissivities of polarized  
353 surfaces, such as open water surfaces, are strongly influenced by the viewing angle, for the cross-track scanning  
354 radiometers the emissivity variation is compensated by the effect of the mixture of the two polarizations (see also  
355 *Felde & Pickle, 1995, Prigent et al, 2000, Mathew et al, 2008, Prigent et al, 2017*).

356 The estimated spectra are shown in Figure 4 and Figure 5 for the land and ocean classes, respectively. It is possible  
357 to observe that the classes are well-characterized from a radiometric point of view, showing distinct behavior of  
358 the emissivity spectra (e.g., the mean values). However, all the classes present significant standard deviations at  
359 high frequency, and some classes - such as the snow classes and the Broken Sea Ice class - present a high value



360 of standard deviation also at low frequency. The coast observations have been also considered as a class, however  
361 its spectrum is not shown in Figures 4-5.

362 The RMSE between simulated clear-sky TBs - based on the mean emissivity values estimated for each class - and  
363 the coincident observed clear-sky TBs appears to be too high to implement a robust signal analysis (>10 K). For  
364 this reason, a refinement process for the emissivity spectra estimation based on machine learning techniques has  
365 been developed downstream of the PESCA classification.

366 The refinement process has been based on a combination of an unsupervised classification technique (SOM) and  
367 a supervised technique (LDA). The unsupervised classification identifies clusters characterized by the minimum  
368 inner variability from a radiometric point of view. The supervised technique, instead, has the goal to identify the  
369 previously obtained clusters, and the associated emissivity spectra, by using only input variables that are not  
370 affected by the presence of clouds. The final emissivity spectra are estimated as the mean emissivity for each  
371 frequency within each cluster identified by the supervised technique. Therefore, as first step, the emissivity value  
372 set has been clustered in order to minimize the emissivity variability in each cluster by arranging the retrieved  
373 emissivity values for six ATMS channels (23.8 GHz, 31.4 GHz, 50.3 GHz, 88.2 GHz, 165.5 GHz, and 183.31±7  
374 GHz) in a one-dimensional SOM architecture. Then, an LDA model has been trained using the previously obtained  
375 clusters as reference and using the PESCA input parameters (**pem<sub>23</sub>**, **pem<sub>31</sub>**, **ratio** and **SI**), some environmental  
376 parameters (**TPW**, **T<sub>2m</sub>**, surface pressure - **P<sub>surf</sub>**) and ancillary variables (latitude - **lat**, Julian day - **jd**, altitude -  
377 **DEM**, the maximum solar height during the day - **H<sub>sun</sub>**) as input. The use of the LDA is necessary to associate an  
378 emissivity spectrum to all the observations which are classified by PESCA, independently from the presence of  
379 clouds. It is worth noticing that the whole predictor set of the LDA has resulted to be redundant; therefore, a subset  
380 of the predictors has been selected for each class. The accuracy of the LDA classification is given by the ratio  
381 between the number of hits (observations where LDA identifies the associated SOM class) and the total number  
382 of observations; it can be considered as an indicator of the effectiveness of the LDA model in rebuilding the SOM  
383 results.

384 The evaluation of the refinement process is based on the comparison between the simulated clear-sky TBs and the  
385 observed clear-sky TBs for each PESCA surface class. An emissivity spectrum, (calculated as the mean of the  
386 emissivity values for each cluster), together with ECMWF temperature and water vapor profiles, is used as input  
387 in the RTM to simulate the clear-sky TBs. For each PESCA surface class, the number of clusters that  
388 simultaneously lowers the errors (RMSE) between the simulated and observed clear-sky TBs at high frequency  
389 (without lowering the classification accuracy too much) is chosen.

390 In Table 2 the number of clusters, the predictors selected, the accuracy, RMSE and percentage normalized root  
391 mean squared error (NRMSE%) (Gareth *et al*, 2013) estimated on the test dataset, are reported for the 165.5 GHz  
392 channel. NRMSE% is defined by Equation 2.

$$393 \text{NRMSE}_{\%} = \left( \frac{\text{RMSE}}{\sigma} * 100 \right)$$

394 (2)

395 where  $\sigma$  represents the standard deviation of the measured clear-sky TBs dataset in each PESCA class. It can be  
396 considered an indicator of the effectiveness of the refinement process.

397 For some classes, such as the Ocean class, the refinement process leads to very low RMSE values ( $\approx 2$  K). For  
398 other classes, such as Deep Dry Snow and Broken Sea Ice, RMSE remains > 5 K even with a high number of  
399 clusters, although there is a significant reduction compared to the initial variance in each class (NRMSE% < 50).  
400 This is due to the variability of snow-covered background within each class; in the worst scenario, the limited  
401 number of predictors are insufficient to infer the emissivity spectrum at high frequency. Overall, the refinement  
402 process allows to obtain a general improvement of the accuracy of the emissivity estimation for the PESCA  
403 classes; however, for some classes, the high-frequency channel uncertainty remains significant.

404 The emissivity spectra obtained by PESCA refinement are used as inputs of the RTM to obtain clear sky simulated  
405 TBs (TB<sub>sim</sub>) to be compared to the actual observations (TB<sub>obs</sub>). The comparison between TB<sub>sim</sub> with TB<sub>obs</sub> allows  
406 to highlight and interpret the MW signal in presence of snowfall.

407 In Figure 6, the snowfall signal is represented as a function of the SWP for the 165.5 GHz channel and for different  
408 PESCA classes. The red line and shaded areas represent the mean values and standard deviations of the difference  
409 between the TB<sub>obs</sub> and the TB<sub>sim</sub> ( $\Delta\text{TB}_{\text{obs-sim}} = \text{TB}_{\text{obs}} - \text{TB}_{\text{sim}}$ ) for SWP bins calculated for observations where 2CSP  
410 SWP > 0 kg m<sup>-2</sup>. The blue lines represent the uncertainty due to surface emissivity variability for each PESCA.  
411 They are centered on the estimated bias for each class (close to 0 K) and the dashed lines correspond to the



412 standard deviation of  $\Delta TB_{\text{obs-sim}}$  in clear sky conditions. A clear scattering signal ( $\Delta TB_{\text{obs-sim}} < 0$ ) is observed over  
413 all the classes considered for intense snowfall events ( $SWP > 1 \text{ kg m}^{-2}$ ). For lower SWP values, the signal is more  
414 ambiguous and changes with the background surface. While over Land there is a clear scattering signal for  $SWP$   
415  $> 0.1 \text{ kg m}^{-2}$ , over the Perennial Snow class a scattering signal can be observed only for  $SWP > 0.5 \text{ kg m}^{-2}$ . For  
416  $SWP < 0.1 \text{ kg m}^{-2}$ , the mean  $\Delta TB_{\text{obs-sim}}$  for snowfall observations is less than its standard deviation in clear sky.  
417 This is due mainly to the emissivity variability for each surface class, and to the error introduced by the use of  
418 model-derived temperature and water vapor profiles in the RT simulations. However, while for the Land class the  
419 mean  $\Delta TB_{\text{obs-sim}} < 0 \text{ K}$  can be explained as a predominant scattering effect for all SWP values, for the Perennial  
420 Snow class the mean  $\Delta TB_{\text{obs-sim}} > 0 \text{ K}$  can be interpreted as a predominant emission signal with respect to the  
421 radiatively cold background (Figure 5). The Thin Snow class shows an intermediate behavior: for  $SWP < 0.1 \text{ kg}$   
422  $\text{m}^{-2}$  the red shaded area within the RMSE limits (blue lines) of the RT simulations denotes the difficulty in  
423 interpreting the signal, while a clear scattering signal can be observed for  $SWP > 0.3 \text{ kg m}^{-2}$ .

### 424 3.2 ANN Design for snowfall retrieval

425 The snowfall detection and estimation modules have been based on ANNs. Four ANNs have been developed: two  
426 for the detection of SWP and SSR and two for the SWP and SSR estimate. The performance of more than 50  
427 architectures have been tested, by varying the number of layers, the number of neurons for each layer, and the  
428 activation functions. The final architecture, for all modules, is composed of four layers: an input layer with a  
429 neurons number equal to the predictor number, and a hyperbolic tangent function as the activation function, a first  
430 hidden layer (60 neurons), and hyperbolic tangent function, a second hidden layer (30 neurons), with a logarithmic  
431 tangent function. At the same time, several predictor sets have been tested combining in different ways ATMS  
432  $TB_{\text{obs}}$ ,  $\Delta TB_{\text{obs-sim}}$ , PESCA surface class, ATMS angle of view, ancillary information (surface elevation from a  
433 Digital Elevation Model), and model-derived environmental variables ( $T_{2m}$ , TPW, and freezing level height). In  
434 Table 3 the statistical scores of the algorithm performance for the SSR detection module obtained for different  
435 predictor sets are reported. It is possible to see that the best performance is obtained when the predictor set is  
436 composed of ATMS  $TB_{\text{obs}}$  and  $\Delta TB_{\text{obs-sim}}$ , (besides PESCA surface flag, the pixel elevation and the cosine of the  
437 viewing angle). In particular, it is possible to observe an improvement of the detection capabilities with respect to  
438 a predictor set composed of ATMS  $TB_{\text{obs}}$  and environmental parameters. This indicates that the computation of  
439 the multi-channel clear-sky TBs at the time of the overpass through the estimation of the PESCA surface class  
440 emissivity spectra and its deviation from the measured TBs, derived from the previous surface radiometric  
441 characterization obtained by PESCA, plays a fundamental role in snowfall retrieval. It provides essential  
442 information to the ANN to be able to exploit the subtle snowfall-related signal in ATMS measurements. This is  
443 the most innovative aspect of HANDEL-ATMS.

444 The final set of predictors is composed by the 16 ATMS  $TB_{\text{obs}}$ , by the  $\Delta TB_{\text{obs-sim}}$  set for the 16 ATMS channels,  
445 from the PESCA classification flag, the pixel elevation (obtained from a DEM) and the cosine of the view angle.

## 446 4. Results

### 447 4.1 HANDEL-ATMS Performances

448 In Table 4 the statistical scores of HANDEL-ATMS detection module performances are reported in terms of  
449 POD, FAR and HSS. It is possible to observe good detection capabilities both for SWP and SSR modules (POD  
450  $> 0.8$ , FAR  $< 0.2$ ).

451 In Figure 7 and in Figure 8 the dependence of HANDEL-ATMS snowfall detection statistical scores on TPW and  
452 on  $T_{2m}$  is reported. In both figures, it is possible to observe that the SWP detection capabilities improve (with an  
453 increase of POD and HSS and a decrease of FAR) with increasing humidity and temperature. This is due to the  
454 combined effect of a stronger scattering signal associated with more intense snowfall events - linked to moister  
455 and warmer environmental conditions - and to the lower transmissivity of the atmosphere which masks the  
456 background surface signal, reducing its impact and the uncertainties linked to its variability. On the other hand,  
457 colder and drier conditions are usually linked to background surface types characterized by high radiometric  
458 variability such as Perennial Snow and Winter Polar Snow classes, which cause uncertainty in emissivity  
459 estimation. It is possible to observe that in Figure 7 SSR detection capabilities show a maximum HSS value for  
460 TPW between 3 mm and 5 mm, and then there is a slight decrease due to the decrease of POD. A similar situation  
461 can be observed in Figure 8, where HANDEL-ATMS SSR HSS reaches a maximum between 250 K and 275 K  
462 and then decreases and it is lower than for SWP. This is due to the fact that PMW measurements respond mostly  
463 to the snow in the atmospheric column and in moister/warmer conditions the presence of snow in the atmosphere



464 is not always linked to surface snowfall. In both cases, it is worth noting that also considering very dry (TPW  $\approx$  2  
465 mm) or very cold ( $T_{2m} \approx$  240 K) conditions, HANDEL-ATMS shows good detection capabilities, in spite of the  
466 uncertainties linked to the modeling of the background surface and the weakness of the signal in such conditions.  
467 Moreover, it is worth noticing that, also considering very low SWP and SSR values (SWP  $\approx$  0.001 kg m<sup>-2</sup>, SSR  
468  $\approx$  0.001 mm h<sup>-1</sup>), HANDEL-ATMS manages to detect around 60 % of the snowfall events. Similar considerations  
469 can be done also for the different background surfaces. The detection capabilities are influenced both by the typical  
470 environmental conditions of each PESCA class and by the uncertainties linked to the emissivity estimation. In  
471 Table 6 the statistical scores of the algorithm performance by considering each PESCA class for both the SWP  
472 and the SSR detection module are reported. It can be observed that, also considering specifically the classes where  
473 the detection is more problematic both for the uncertainties linked to the emissivity retrieval (see Table 2), for the  
474 extremely dry and cold environmental conditions, and for the low intensity of the snowfall events, such as  
475 Perennial Snow or Winter Polar Snow, HANDEL-ATMS has good detection capabilities (POD and FAR values  
476 greater than 0.7 and less than 0.25, respectively, for both SWP and SSR). These results provide evidence that  
477 HANDEL-ATMS can be used to analyze snowfall occurrence in the polar regions.  
478 The error statistics of the two estimation modules are reported in Table 5 in terms of bias, RMSE and the  
479 coefficient of determination  $R^2$ , which is defined by Equation 3.

$$480 \quad R^2 = 1 - \frac{RMSE^2}{std^2}$$

481 (3)

482 It is worth noticing that the biases are negligible for both modules while RMSE values are comparable to the light  
483 events recorded in the dataset. Moreover, RMSE and  $R^2$  values are respectively higher and lower for the SSR  
484 module than for the SWP module; this is due to the fact that the PMW signature is mainly related to the presence  
485 of snow in the atmosphere rather than to the surface snowfall rate. In Figure 9 the density scatterplots between the  
486 SWP and SSR values retrieved by HANDEL-ATMS and the 2CSP corresponding values are reported. For both  
487 modules, an overestimation can be observed for very light snowfall (SWP < 10<sup>-2</sup> kg m<sup>-2</sup> and SSR < 10<sup>-2</sup> mm h<sup>-1</sup>),  
488 while there is a very good agreement for higher SWP and SSR values.

489 . Generally, it can be observed that, although HANDEL-ATMS is able to detect extremely light snowfall events,  
490 it does not have the sensitivity to correctly estimate their intensity.

#### 491 **4.2 A Case Study: Greenland-2016/04/24**

492 The case study reported corresponds to the observation of a moderately light snowfall event over the central part  
493 of Greenland that occurred on 24 April 2016. ATMS overpass is between 14:51:23 U.T.C. and 14:57:47 U.T.C.,  
494 while the CPR overpass is between 15:05:25 U.T.C. and 15:11:45 U.T.C., with a time difference of 14 minutes  
495 and 2 seconds. This event presents several characteristics typical of high latitudes, such as light snowfall rate, dry  
496 and cold atmospheric conditions, and presence of a frozen background surface, a typical case of interest for the  
497 application of HANDEL-ATMS.

498 In Figure 10 PESCA classification is reported. The entire territory of Greenland, except for a narrow area on the  
499 southwestern coast, is identified as a snow-covered surface; PESCA identifies the Perennial Snow class in the  
500 central part of Greenland and along CloudSat track and the Polar Winter Snow class near the northern shoreline.  
501 CloudSat overpasses the central part of the island, and CPR track is along the central part of the ATMS swath.

502 In Figure 11 a synopsis of the event along the CPR track is reported: the environmental parameters,  $T_{2m}$  and TPW,  
503 the 2CSP SWP and SSR values, the cross-section of CPR reflectivity, with the DARDAR supercooled water  
504 information superimposed (in magenta). Moreover, the PESCA surface classification, and the TBs of the main  
505 ATMS high-frequency channels along the CloudSat track are reported. The event is characterized by dry  
506 conditions (TPW < 5 mm) and  $T_{2m}$  below 273 K, except over the coast. CPR observes a cloud system linked to  
507 the snowfall event between 68 °N and 76 °N; DARDAR detects the presence of a supercooled water layer at the  
508 cloud top between 68 °N and 72 °N and indicates the presence of supercooled droplets embedded in the deeper  
509 cloud associated to the more intense snowfall. 2CSP detects a light snowfall event in the inner part of the island  
510 and a more intense event, with a peak of intensity between 72 °N and 76 °N, near the shoreline. For what concerns  
511 the associated ATMS observations, an increase of the 88 GHz and 165 GHz TBs is observed in coincidence with  
512 the supercooled water layer; on the other hand, only a slight decrease of 165.5 and 183.3+7 GHz TBs can be  
513 observed in coincidence with the snowfall intensity peak.



514 In figure 12 the maps of the  $TB_{obs}$  at 165.5 GHz (top panel) and the  $\Delta TB_{obs-sim}$  at 165.5 GHz (bottom panel) are  
515 reported. In the top panel, it is possible to observe that, despite the snowfall event, there is not a clear TB scattering  
516 signal in the area where 2CSP detects snowfall (70 °N -76 °N, 40 °W -70 °W); instead a slight increase in the TBs  
517 can be observed in the area where DARDAR detects the supercooled water layer. The simulation of the clear-sky  
518 TBs ( $TB_{sim}$ ) allows to observe an emission signal ( $\Delta TB_{obs-sim} > 0$ ) over the central part of the ATMS swath due to  
519 the combined effect of supercooled liquid water emission (as evidenced by DARDAR supercooled water layers)  
520 and radiatively cold surface background. Only near the shoreline, the  $TB_{obs}$  is slightly lower than the  $TB_{sim}$   
521 ( $\Delta TB_{obs-sim} < 0$ ). In Figure 13 the results of the HANDEL-ATMS four modules are reported. It is worth noting  
522 that both detection modules find snowfall in the central region of Greenland and near the northern coast. The  
523 estimated intensity of this event is generally light ( $SWP < 0.1 \text{ kg m}^{-2}$  and  $SSR < 0.1 \text{ mm h}^{-1}$ ) except over the  
524 western coast, where  $SWP$  reaches  $0.5 \text{ kg m}^{-2}$  and  $SSR$  reaches  $1 \text{ mm h}^{-1}$ . It is worth noticing that HANDEL-  
525 ATMS detects snowfall also where there is an emission signal ( $\Delta TB_{obs-sim} > 0$ ).  
526 Finally, a comparison between the HANDEL-ATMS and the 2CSP is reported in Figure 14. It is worth noting that  
527 there is a substantial agreement on the snowfall detection of the two products. It can be observed that HANDEL-  
528 ATMS tends to overestimate both  $SWP$  and  $SSR$  in presence of very light snowfall (2CSP  $SWP < 0.05 \text{ kg m}^{-2}$   
529 and  $SSR < 0.1 \text{ mm h}^{-1}$ , between 68 °N and 72 °N), consistently with what shown in Fig. 9; on the other hand,  
530 there is a good agreement between 72 °N and 76 °N, where snowfall intensity increases.  
531 The analysis of this case study demonstrates that the algorithm can interpret the ambiguity of the  
532 emission/scattering signal associated with snowfall described in Section 4.1 and so efficiently detect and quantify  
533 snowfall even in extreme conditions.

#### 534 4.3 Comparison with SLALOM-CT

535 SLALOM-CT has been introduced in Section 1. It presents some similarities with HANDEL-ATMS: it is based  
536 on an ANN approach and uses CPR-2CSP product as reference. On the other hand, substantial differences have  
537 to be highlighted: SLALOM-CT was designed to operate on a global scale, while HANDEL-ATMS has been  
538 developed specifically for the extreme conditions typical of high latitudes. Moreover, the predictor sets are  
539 different: in addition to TB observations, SLALOM-CT relies on several model derived environmental  
540 parameters, while HANDEL-ATMS relies on differences between simulated clear-sky TBs and observed TBs  
541 ( $\Delta TB_{obs-sim}$ ), and therefore on the estimation of the background surface emissivity at the time of the overpass, as  
542 described in Section 3.

543 In Table 7 a comparison between the statistical scores of the detection performances of the two algorithms is  
544 reported for different environmental conditions. The comparison has been carried out considering the same  
545 observations of the ATMS-CPR coincidence dataset. It can be observed that, as in colder and drier conditions, the  
546 differences between the two algorithm performances increase: HANDEL-ATMS shows better snowfall detection  
547 capabilities than SLALOM-CT. Considering the working limits of HANDEL-ATMS, POD increases by 2 % and  
548 FAR decreases by 8 %; however, if only very cold/dry conditions are considered ( $T_{2m} < 250 \text{ K}$ ,  $TPW < 5 \text{ mm}$ ),  
549 POD increases by 7 % and FAR decreases by 16 %; for extremely dry/cold conditions ( $T_{2m} < 240 \text{ K}$ ,  $TPW < 3$   
550 mm), typical of the inner part of Greenland and Antarctica, POD increases by 18 % and FAR decreases by 16 %.

#### 551 5 Conclusions and Future Perspectives

552 In this paper a new snowfall retrieval algorithm, the High Latitude sNow Detection and Estimation aLgorithm for  
553 ATMS (HANDEL-ATMS), is described. The algorithm is based on machine learning techniques, and it has been  
554 trained against CPR snowfall products. It has been developed specifically for the extreme conditions typical of  
555 high latitude regions. The driving and innovative principle in the algorithm development is the exploitation of  
556 the full range of ATMS channel frequencies to characterize the frozen background surface radiative properties at  
557 the time of the overpass to be able to better isolate and interpret the snowfall-related contribution to the measured  
558 multi-channel upwelling radiation. This approach is proven to be effective for snowfall detection and  
559 quantification at high latitudes, particularly in presence of a frozen (snow-covered land or sea ice) background,  
560 also compared to other state-of-the art machine learning based methods.

561 HANDEL-ATMS can detect snowfall at high latitudes in good agreement with CPR. The estimation modules tend  
562 to overestimate the intensity of light snowfall events ( $SWP < 10^{-2} \text{ kg m}^{-2}$ ) but it shows good accuracy for more  
563 intense snowfall events ( $SWP > 10^{-2} \text{ kg m}^{-2}$ ,  $SWP < 1 \text{ kg m}^{-2}$ ). It is worth noting, however, that the uncertainty  
564 associated with the surface emissivity estimation in some conditions affects the capabilities of HANDEL-ATMS  
565 to correctly interpret the snowfall signature. Such uncertainty, related to the difficulty in correctly modeling the



566 intrinsic variability of snow cover surface emissivity, propagates in the radiative transfer simulation of the clear-  
567 sky TBs used as input in the algorithm. Despite these limitations, it is worth noticing that the development of an  
568 algorithm capable of retrieving snowfall at high-latitudes conditions with good accuracy is an important  
569 development in the climate science field. The possibility to exploit a big amount of data guaranteed by near-polar  
570 operational satellites carrying ATMS radiometers allows obtaining snowfall estimates characterized by a full  
571 coverage of the polar areas and a high temporal resolution. Moreover, the future European MetOp Second  
572 Generation (MetOp-SG) mission, with the launch of the Sat-A Microwave Sounder (MWS), with characteristics  
573 very similar to ATMS, will provide another instrument to improve global snowfall monitoring. The HANDEL  
574 methodology will be also adapted to be able to exploit MWS measurements in the future. The possibility to exploit  
575 a wide range of microwave channels allows obtaining a characterization of the background surface at the time of  
576 the overpass. This element is fundamental to obtain a characterization of the snowfall signature (especially for the  
577 extreme environmental conditions typical of high latitudes), and an accurate snowfall retrieval. The capability to  
578 estimate snowfall events with a high temporal resolution is ancillary to the development of a continuous snowfall  
579 monitoring system over the high latitude areas and to analyze the snowfall climatology in these areas. This  
580 research could have important impacts in climate change studies; snowfall is predominant over rain in the high-  
581 latitude areas, and it has been proven that climate change has a strong impact on snowfall regime in these areas.  
582 Future research activities will tackle some open issues. The estimation of the surface emissivity and the simulated  
583 clear-sky multi-channel TBs needs to be further improved, either by considering other predictor sets or by using  
584 a different technique for the emissivity spectra refinement process, or by using more advanced radiative transfer  
585 models. Another important aspect is the quantification of the error linked to the background emissivity estimation  
586 on the snowfall detection capabilities. This would be also useful for the development of modules for mountainous  
587 areas, which have not been analyzed in this study. Moreover, the effect on the algorithm snowfall detection  
588 capabilities of the uncertainties linked to the model-derived environmental variables (e.g., temperature and water  
589 vapor profile), which are used in the clear-sky TB simulations, should be investigated. The use of the ATMS water  
590 vapor (183 GHz band) and temperature (50 GHz band) sounding channels to characterize the atmospheric  
591 conditions at the time of the overpass in order to avoid the use of model-derived data is another subject of future  
592 research. Moreover, the possible development of a separate supercooled liquid water detection module could also  
593 be evaluated, similarly to what is done in other PMW snowfall detection and estimation algorithms (*Rysman et*  
594 *al., 2018, Sanò et al., 2022*). Such information can be exploited to improve snowfall detection and estimation  
595 capabilities since the emission by the cloud droplets in dry conditions tends to mask the snowfall scattering signal  
596 (see *Panegrossi et al, 2017, Panegrossi et al, 2022*), and adds larger uncertainties in the CPR snowfall products  
597 (*Battaglia & Panegrossi, 2021*). Finally, since the algorithm has been developed only for specific environmental  
598 conditions typical of high latitudes (dry and cold atmosphere) an integration with other approaches, such as  
599 SLALOM-CT, designed for global estimation of snowfall, could be considered in the future to improve global  
600 snowfall monitoring based on ATMS and future cross-track scanning radiometers.

#### 601 602 **Data availability**

603 ATMS data are provided by the NOAA CLASS facility [www.avl.class.noaa.gov/](http://www.avl.class.noaa.gov/) (last access 4 april 2023), CPR  
604 data are distributed by the CloudSat data processing center <https://www.cloudsat.cira.colostate.edu/> (last access  
605 4 april 2023), DARDAR data are available from the ICARE FTP server of the University of Lille ([ftp.icare.univ-](ftp.icare.univ-lille1.fr)  
606 [lille1.fr](ftp.icare.univ-lille1.fr), last access 4 april 2023) and ECMWF operational forecasts are distributed by ECMWF through the  
607 MARS facility via the ECGATE cluster. AutoSonw data are provided by the NOAA Satellite and Information  
608 Service [https://satepsanone.nesdis.noaa.gov/northern\\_hemisphere\\_multisensor.html](https://satepsanone.nesdis.noaa.gov/northern_hemisphere_multisensor.html) (last access 4 april 2023).

#### 609 **Author Contribution**

610 Conceptualization, A.C., P.S., D.C.; methodology, A.C., P.S., D.C.; software, A.C.; validation, A.C.; formal  
611 analysis, A.C.; investigation, A.C., P.S., D.C., G.P.; data curation, A.C. and D.C.; writing—original draft  
612 preparation, A.C.; writing—review and editing, A.C., P.S., D.C., and G.P.; visualization, A.C.; supervision, G.P.;  
613 project administration, G.P.; funding acquisition, G.P. All authors have read and agreed to the published version  
614 of the manuscript.

#### 615 **Competing Interests**

616 The authors declare no conflict of interest. The funders had no role in the design of the study; in the collection,  
617 analyses, or interpretation of data; in the writing of the manuscript, or in the decision to publish the results.



618 **Acknowledgements**

619 This work was carried out under the RainCast study (ESA Contract No. 4000125959/18/NL/NA) and by the  
620 EUMETSAT Satellite Application Facility for Operational Hydrology and Water management (H SAF) Fourth  
621 Continuous and Operations Phase (CDOP-4). Andrea Camplani was supported by the Ph.D. program in  
622 Infrastructures, Transport Systems and Geomatics at the Department of Civil, Constructional, and Environmental  
623 Engineering at Sapienza University of Rome. The authors would like to thank EUMETSAT and the NASA  
624 Precipitation Measurement Mission (PMM) Research Program for supporting scientific collaborations between H  
625 SAF and GPM, and the PMM Science Team. The authors wish to express their sincere gratitude to Joe Turk  
626 (NASA JPL) and Alessandro Battaglia are warmly acknowledged for useful interactions and discussions during  
627 the algorithm development and validation and to Mattia Crespi for the scientific support to Andrea Camplani  
628 during the Ph.D. program.

629 **References**

- 630 Battaglia, A., & Delanoë, J.: Synergies and complementarities of CloudSat-CALIPSO snow observations. *Journal*  
631 *of Geophysical Research: Atmospheres*, 118(2), 721-731. <https://doi.org/10.1029/2012JD018092>, 2013.
- 632 Battaglia, A., & Panegrossi, G.: What can we learn from the CloudSat radiometric mode observations of snowfall  
633 over the ice-free ocean? *Remote Sensing*, 12(20), 3285, <https://doi.org/10.3390/rs12203285>, 2020.
- 634 Behrangi, A., Christensen, M., Richardson, M., Lebsock, M., Stephens, G., Huffman, G. J., Bolvin, D., Adler, R.  
635 F., Gardner, A., Lambrightsten, B., & Fetzer, E.: Status of high-latitude precipitation estimates from observations  
636 and reanalyses. *Journal of Geophysical Research: Atmospheres*, 121(9), 4468-4486,  
637 <https://doi.org/10.1002/2015JD024546>, 2016.
- 638 Bintanja, R., Selten, F.: Future increases in Arctic precipitation linked to local evaporation and sea-ice retreat.  
639 *Nature* 509, 479-482, <https://doi.org/10.1038/nature13259>, 2014.
- 640 Camplani, A., Casella, D., Sanò, P., & Panegrossi, G.: The Passive microwave Empirical cold Surface  
641 Classification Algorithm (PESCA): Application to GMI and ATMS. *Journal of Hydrometeorology*, 22(7), 1727-  
642 1744, <https://doi.org/10.1175/JHM-D-20-0260.1>, 2021.
- 643 Casella, D., Panegrossi, G., Sanò, P., Marra, A. C., Dietrich, S., Johnson, B. T., & Kulie, M. S.: Evaluation of the  
644 GPM-DPR snowfall detection capability: Comparison with CloudSat-CPR. *Atmospheric Research*, 197, 64-75,  
645 <https://doi.org/10.1016/j.atmosres.2017.06.018>, 2017.
- 646 Ceccaldi, M., Delanoë, J., Hogan, R. J., Pounder, N. L., Protat, A., & Pelon, J.: From CloudSat-CALIPSO to  
647 EarthCare: Evolution of the DARDAR cloud classification and its comparison to airborne radar-lidar  
648 observations. *Journal of Geophysical Research: Atmospheres*, 118(14), 7962-7981,  
649 <https://doi.org/10.1002/jgrd.50579>, 2013.
- 650 DARDAR- retrieve cloud properties by combining the CloudSat radar and the CALIPSO lidar measurements.  
651 CNS-CNRS-Université de Lille., <https://www.icare.univ-lille.fr/dardar/>, last access: 4 April 2023.
- 652 Clifford, D.: Global estimates of snow water equivalent from passive microwave instruments: history, challenges  
653 and future developments. *International Journal of Remote Sensing*, 31(14), 3707-3726,  
654 <https://doi.org/10.1080/01431161.2010.483482>, 2010.
- 655 Comiso, J. C.: Sea ice effective microwave emissivities from satellite passive microwave and infrared  
656 observations. *Journal of Geophysical Research: Oceans*, 88(C12), 7686-7704.  
657 <https://doi.org/10.1029/JC088iC12p07686>, 1983
- 658 Cordisco, E., Prigent, C., & Aires, F.: Snow characterization at a global scale with passive microwave satellite  
659 observations. *Journal of Geophysical Research: Atmospheres*, 111(D19), <https://doi.org/10.1029/2005JD006773>,  
660 2006.
- 661 Fausett, L. V., Fundamentals of neural networks: architectures, algorithms and applications, Pearson Education  
662 India, ISBN-13: 978-0133341867, 1994.
- 663 Felde, G. W., & Pickle, J. D.: Retrieval of 91 and 150 GHz Earth surface emissivities. *Journal of Geophysical*  
664 *Research: Atmospheres*, 100(D10), 20855-20866, <https://doi.org/10.1029/95JD02221>, 1995.
- 665 Gareth, J., Daniela, W., Trevor, H., & Robert, T.: An introduction to statistical learning: with applications in R.  
666 Springer, ISBN-13:978-1461471370 , 2013.
- 667 Grody, N. C., & Basist, A. N.: Global identification of snowcover using SSM/I measurements. *IEEE Transactions*  
668 *on geoscience and remote sensing*, 34(1), 237-249, DOI: 10.1109/36.481908, 1996.



- 669 Hastie, T., Tibshirani, R., Friedman, J. H., & Friedman, J. H.: *The elements of statistical learning: data mining,*  
670 *inference, and prediction* (Vol. 2, pp. 1-758). New York: springer, DOI: 10.1007/b94608, 2009.
- 671 Kidd, C., & Huffman, G.: Global precipitation measurement. *Meteorological Applications*, 18(3), 334-353,  
672 <https://doi.org/10.1002/met.284>, 2011.
- 673 Hewison, T. J., & English, S. J.: Airborne retrievals of snow and ice surface emissivity at millimeter wavelengths.  
674 *IEEE Transactions on Geoscience and Remote Sensing*, 37(4), 1871-1879, DOI: 10.1109/36.774700, 1999.
- 675 Kim, M. J., Weinman, J. A., Olson, W. S., Chang, D. E., Skofronick-Jackson, G., & Wang, J. R.: A physical  
676 model to estimate snowfall over land using AMSU-B observations. *Journal of Geophysical Research:*  
677 *Atmospheres*, 113(D9), <https://doi.org/10.1029/2007JD008589>, 2008.
- 678 Kohonen, T.: *Self-organization and associative memory* (Vol. 8). Springer Science & Business Media,  
679 DOI:10.1007/978-3-642-88163-3, 2012.
- 680 Kongoli, C., Pellegrino, P., Ferraro, R. R., Grody, N. C., & Meng, H.: A new snowfall detection algorithm over  
681 land using measurements from the Advanced Microwave Sounding Unit (AMSU). *Geophysical Research Letters*,  
682 30(14), <https://doi.org/10.1029/2003GL017177>, 2003.
- 683 Kongoli, C., Meng, H., Dong, J., & Ferraro, R.: A snowfall detection algorithm over land utilizing high-frequency  
684 passive microwave measurements—Application to ATMS. *Journal of Geophysical Research: Atmospheres*,  
685 120(5), 1918-1932, <https://doi.org/10.1002/2014JD022427>, 2015.
- 686 Kongoli, C., Meng, H., Dong, J., & Ferraro, R.: A hybrid snowfall detection method from satellite passive  
687 microwave measurements and global forecast weather models. *Quarterly Journal of the Royal Meteorological*  
688 *Society*, 144, 120-132. <https://doi.org/10.1002/qj.3270>, 2018.
- 689 Kulie, M. S., Bennartz, R., Greenwald, T. J., Chen, Y., & Weng, F.: Uncertainties in microwave properties of  
690 frozen precipitation: Implications for remote sensing and data assimilation. *Journal of the Atmospheric Sciences*,  
691 67(11), 3471-3487. <https://doi.org/10.1175/2010JAS3520.1>, 2010.
- 692 Kulie, M. S., Milani, L., Wood, N. B., Tushaus, S. A., Bennartz, R., & L'Ecuyer, T. S.: A shallow cumuliform  
693 snowfall census using spaceborne radar. *Journal of Hydrometeorology*, 17(4), 1261-1279.  
694 <https://doi.org/10.1175/JHM-D-15-0123.1>, 2016.
- 695 Levizzani, V., Laviola, S., & Cattani, E.: Detection and measurement of snowfall from space. *Remote Sensing*,  
696 3(1), 145-166, <https://doi.org/10.3390/rs3010145>, 2011.
- 697 Liu, Y., Key, J. R., Liu, Z., Wang, X., & Vavrus, S. J.: A cloudier Arctic expected with diminishing sea ice.  
698 *Geophysical Research Letters*, 39(5). <https://doi.org/10.1029/2012GL051251>, 2012.
- 699 Liu, J., Curry, J. A., Wang, H., Song, M., & Horton, R. M.: Impact of declining Arctic sea ice on winter snowfall.  
700 *Proceedings of the National Academy of Sciences*, 109(11), 4074-4079. <https://doi.org/10.1073/pnas.1114910109>,  
701 2012.
- 702 Liu, G., & Seo, E. K.: Detecting snowfall over land by satellite high-frequency microwave observations: The lack  
703 of scattering signature and a statistical approach. *Journal of geophysical research: atmospheres*, 118(3), 1376-  
704 1387, <https://doi.org/10.1002/jgrd.50172>, 2013.
- 705 Mathew, N., Heygster, G., Melsheimer, C., & Kaleschke, L.: Surface emissivity of Arctic sea ice at AMSU  
706 window frequencies. *IEEE transactions on geoscience and remote sensing*, 46(8), 2298-2306,  
707 DOI: [10.1109/TGRS.2008.916630](https://doi.org/10.1109/TGRS.2008.916630), 2008.
- 708 Mätzler, C., & Hüppi, R.: Review of signature studies for microwave remote sensing of snowpacks. *Advances in*  
709 *Space Research*, 9(1), 253-265, [https://doi.org/10.1016/0273-1177\(89\)90493-6](https://doi.org/10.1016/0273-1177(89)90493-6), 1989.
- 710 Meng, H., Dong, J., Ferraro, R., Yan, B., Zhao, L., Kongoli, C., Wang, N., & Zavadsky, B.: A 1DVAR-based  
711 snowfall rate retrieval algorithm for passive microwave radiometers. *Journal of Geophysical Research:*  
712 *Atmospheres*, 122(12), 6520-6540. <https://doi.org/10.1002/2016JD026325>, 2017.
- 713 Milani, L., Kulie, M. S., Casella, D., Dietrich, S., L'Ecuyer, T. S., Panegrossi, G., Porcù, F., Sanò, P., & Wood,  
714 N. B.: CloudSat snowfall estimates over Antarctica and the Southern Ocean: An assessment of independent  
715 retrieval methodologies and multi-year snowfall analysis. *Atmospheric research*, 213, 121-135,  
716 <https://doi.org/10.1016/j.atmosres.2018.05.015>, 2018.
- 717 Milani, L., & Wood, N. B.: Biases in cloudsat falling snow estimates resulting from daylight-only operations.  
718 *Remote Sensing*, 13(11), 2041, <https://doi.org/10.3390/rs13112041>, 2021.



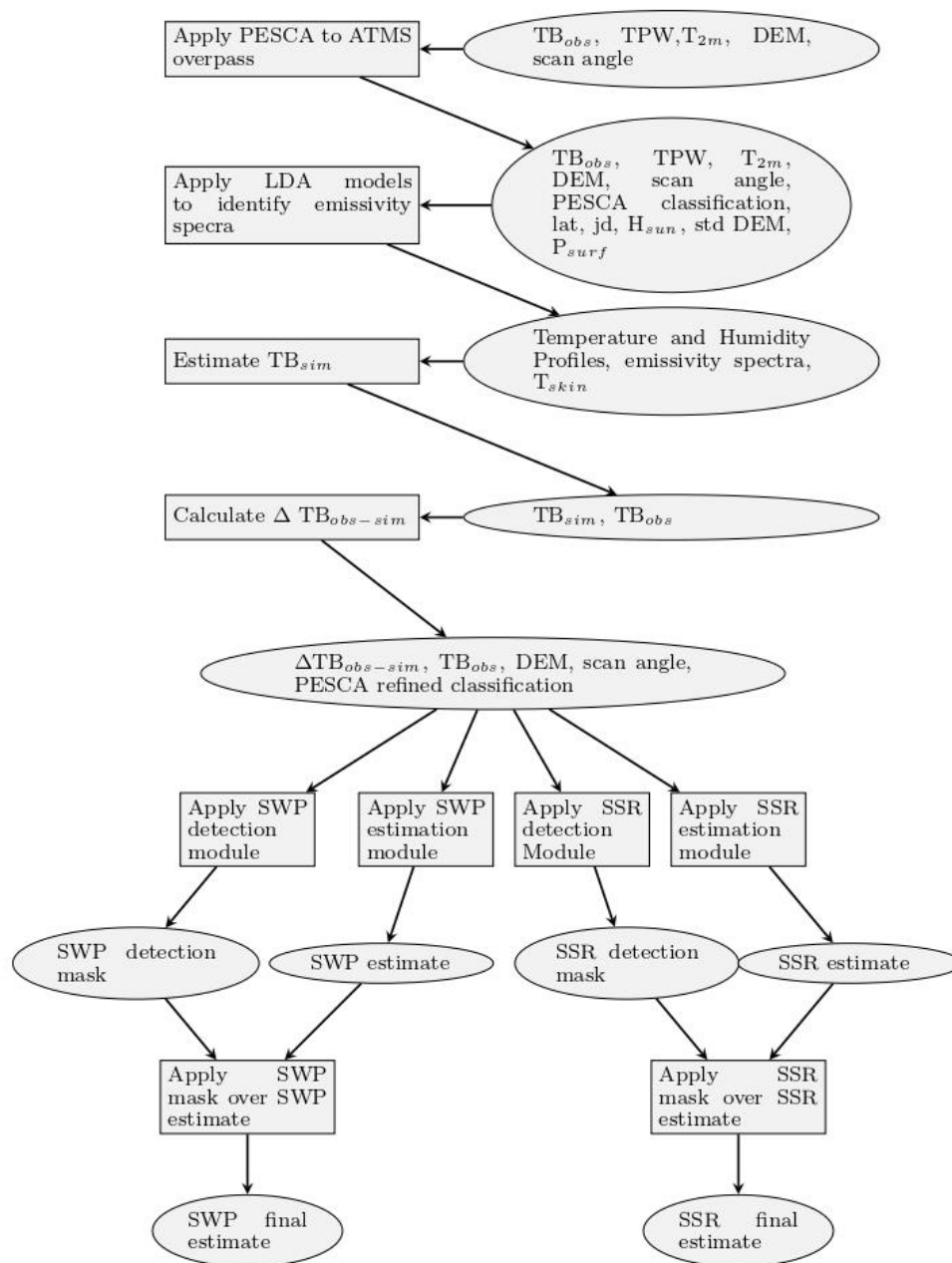
- 719 Mroz, K., Montopoli, M., Battaglia, A., Panegrossi, G., Kirstetter, P., & Baldini, L.: Cross validation of active  
720 and passive microwave snowfall products over the continental United States. *Journal of Hydrometeorology*, 22(5),  
721 1297-1315. <https://doi.org/10.1175/JHM-D-20-0222.1>, 2021.
- 722 Munchak, S. J., Ringerud, S., Brucker, L., You, Y., de Gelis, I., & Prigent, C.: An active–passive microwave land  
723 surface database from GPM. *IEEE Transactions on Geoscience and Remote Sensing*, 58(9), 6224-6242, DOI:  
724 10.1109/TGRS.2020.2975477, 2020.
- 725 Noh, Y. J., Liu, G., Jones, A. S., & Vonder Haar, T. H.: Toward snowfall retrieval over land by combining satellite  
726 and in situ measurements. *Journal of Geophysical Research: Atmospheres*, 114(D24),  
727 <https://doi.org/10.1029/2009JD012307>, 2009.
- 728 Panegrossi, G., Rysman, J. F., Casella, D., Marra, A. C., Sanò, P., & Kulie, M. S.: CloudSat-based assessment of  
729 GPM Microwave Imager snowfall observation capabilities. *Remote Sensing*, 9(12), 1263,  
730 <https://doi.org/10.3390/rs9121263>, 2017.
- 731 Panegrossi, G., Casella, D., Sanò, P., Camplani, A., & Battaglia, A.: Recent advances and challenges in satellite-  
732 based snowfall detection and estimation. *Precipitation Science*, 333-376, <https://doi.org/10.1016/B978-0-12-822973-6.00015-9>, 2022.
- 734 Partaiain, P.: CloudSat ECMWF-AUX Auxiliary Data Product Process Description and Interface Control  
735 Document, Product Version P1\_R05, NASA JPL CloudSat project document revision 0, pp. 16, Available from:  
736 [https://www.cloudsat.cira.colostate.edu/cloudsat-static/info/dl/ecmwf-aux/ECMWF-  
737 AUX.PDICD.P1\\_R05.rev0.pdf](https://www.cloudsat.cira.colostate.edu/cloudsat-static/info/dl/ecmwf-aux/ECMWF-AUX.PDICD.P1_R05.rev0.pdf), 2022
- 738 Prigent, C., Wigneron, J. P., Rossow, W. B., & Pardo-Carrion, J. R.: Frequency and angular variations of land  
739 surface microwave emissivities: Can we estimate SSM/T and AMSU emissivities from SSM/I emissivities?. *IEEE  
740 transactions on geoscience and remote sensing*, 38(5), 2373-2386, DOI:10.1109/36.868893, 2000.
- 741 Prigent, C., Aires, F., Rossow, W., & Matthews, E.: Joint characterization of vegetation by satellite observations  
742 from visible to microwave wavelengths: A sensitivity analysis. *Journal of Geophysical Research: Atmospheres*,  
743 106(D18), 20665-20685, <https://doi.org/10.1029/2000JD900801>, 2001.
- 744 Prigent, C., Jaumouille, E., Chevallier, F., & Aires, F.: A parameterization of the microwave land surface  
745 emissivity between 19 and 100 GHz, anchored to satellite-derived estimates. *IEEE Transactions on Geoscience  
746 and Remote Sensing*, 46(2), 344-352, DOI: 10.1109/TGRS.2007.908881, 2008.
- 747 Prigent, C., Aires, F., Wang, D., Fox, S., & Harlow, C.: Sea-surface emissivity parametrization from microwaves  
748 to millimetre waves. *Quarterly Journal of the Royal Meteorological Society*, 143(702), 596-605.  
749 <https://doi.org/10.1002/qj.2953>, 2017.
- 750 Rahimi, R., Ebtehaj, A., Panegrossi, G., Milani, L., Ringerud, S. E., & Turk, F. J., Vulnerability of Passive  
751 Microwave Snowfall Retrievals to Physical Properties of Snowpack: A Perspective From Dense Media Radiative  
752 Transfer Theory. *IEEE Transactions on Geoscience and Remote Sensing*, 60, 1-13,  
753 <https://doi.org/10.3390/rs11192200>, 2017.
- 754 Romanov, P.: Global multisensor automated satellite-based snow and ice mapping system (GMASI) for  
755 cryosphere monitoring. *Remote Sensing of Environment*, 196, 42-55, <https://doi.org/10.1016/j.rse.2017.04.023>,  
756 2017.
- 757 Rysman, J. F., Panegrossi, G., Sanò, P., Marra, A. C., Dietrich, S., Milani, L., & Kulie, M. S.: SLALOM: An all-  
758 surface snow water path retrieval algorithm for the GPM Microwave Imager. *Remote Sensing*, 10(8), 1278,  
759 <https://doi.org/10.3390/rs10081278>, 2018.
- 760 Rysman, J. F., Panegrossi, G., Sano, P., Marra, A. C., Dietrich, S., Milani, L., Kulie, M. S., Casella, D., Camplani,  
761 A., Claud, C., & Edel, L.: Retrieving surface snowfall with the GPM Microwave Imager: A new module for the  
762 SLALOM algorithm. *Geophysical Research Letters*, 46(22), 13593-13601,  
763 <https://doi.org/10.1029/2019GL084576>, 2019.
- 764 Sanò, P., Casella, D., Camplani, A., D'Adderio, L. P., & Panegrossi, G., A Machine Learning Snowfall Retrieval  
765 Algorithm for ATMS. *Remote Sensing*, 14(6), 1467, <https://doi.org/10.3390/rs14061467>, 2022.
- 766 Sanò, P., Panegrossi, G., Casella, D., Di Paola, F., Milani, L., Mugnai, A., Petracca, M., & Dietrich, S. (2015).  
767 The Passive microwave Neural network Precipitation Retrieval (PNPR) algorithm for AMSU/MHS observations:  
768 description and application to European case studies. *Atmospheric Measurement Techniques*, 8(2), 837-857,  
769 <https://doi.org/10.5194/amt-8-837-2015>, 2015.



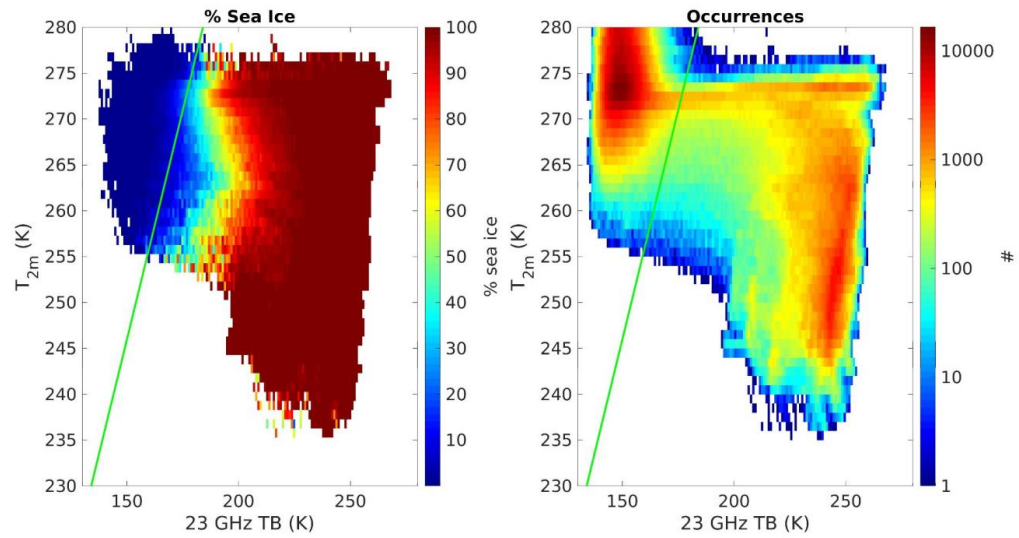
- 770 Skofronick-Jackson, G. M., Kim, M. J., Weinman, J. A., & Chang, D. E. (2004). A physical model to determine  
771 snowfall over land by microwave radiometry. *IEEE Transactions on Geoscience and Remote Sensing*, 42(5),  
772 1047-1058, DOI:10.1109/TGRS.2004.825585, 2004.
- 773 Skofronick-Jackson, G., Hudak, D., Petersen, W., Nesbitt, S. W., Chandrasekar, V., Durden, S., Kristin, J. G.,  
774 Huang, G., Joe, P., Kollias, P., Reed, K., A., Schwaller, M., R., Stewart, R., Tanelli, S., Tokay, A., Wang, J., R.,  
775 & Wolde, M.: Global precipitation measurement cold season precipitation experiment (GCPEX): For  
776 measurement's sake, let it snow. *Bulletin of the American Meteorological Society*, 96(10), 1719-1741,  
777 <https://doi.org/10.1175/BAMS-D-13-00262.1>, 2015.
- 778 Stephens, G. L., Vane, D. G., Tanelli, S., Im, E., Durden, S., Rokey, M., Reinke, D., Partain, P., Mace, G. G.,  
779 Austin, R., L'Ecuyer, T., Haynes, J., Lebsock, M., Suzuki, K., Waliser, D., Wu, D., Kay, J., Gettelman, A., Zhi  
780 Wang, Z., & Marchand, R.: CloudSat mission: Performance and early science after the first year of operation.  
781 *Journal of Geophysical Research: Atmospheres*, 113(D8), <https://doi.org/10.1029/2008JD009982>, 2008.
- 782 Takbiri, Z., Ebtehaj, A., Fofoula-Georgiou, E., Kirstetter, P. E., & Turk, F. J.: A prognostic nested k-nearest  
783 approach for microwave precipitation phase detection over snow cover. *Journal of hydrometeorology*, 20(2), 251-  
784 274, <https://doi.org/10.1175/JHM-D-18-0021.1>, 2019.
- 785 Turk, F. J., Ringerud, S. E., Camplani, A., Casella, D., Chase, R. J., Ebtehaj, A., Gong, J., Kulie, M., Liu, G.,  
786 Milani, L., Panegrossi, G., Padullés, R., Rysman, J. F., Sanò, P., Vahedizade, S., & Wood, N. B.: Applications of  
787 a CloudSat-TRMM and CloudSat-GPM satellite coincidence dataset. *Remote Sensing*, 13(12), 2264,  
788 <https://doi.org/10.3390/rs13122264>, 2021a.
- 789 Turk, F. J., Ringerud, S. E., You, Y., Camplani, A., Casella, D., Panegrossi, G., Sanò, P., Ebtehaj, A., Guilloteau,  
790 C., Utsumi, N., Prigent, C., & Peters-Lidard, C.: Adapting passive microwave-based precipitation algorithms to  
791 variable microwave land surface emissivity to improve precipitation estimation from the GPM constellation.  
792 *Journal of Hydrometeorology*, 22(7), 1755-1781, <https://doi.org/10.1175/JHM-D-20-0296.1>, 2021.
- 793 Ulaby, F., & Long, D., Microwave radar and radiometric remote sensing, 1st Edition, the Univ. of Michigan Press,  
794 ISBN: 978-0-472-11935-6, 2014.
- 795 Vihma, T., Screen, J., Tjernström, M., Newton, B., Zhang, X., Popova, V., Deser, C., Holland, M., & Prowse, T.:  
796 The atmospheric role in the Arctic water cycle: A review on processes, past and future changes, and their impacts.  
797 *Journal of Geophysical Research: Biogeosciences*, 121(3), 586-620, <https://doi.org/10.1002/2015JG003132>,  
798 2016.
- 799 Weng, F., Zou, X., Wang, X., Yang, S., & Goldberg, M. D.: Introduction to Suomi national polar-orbiting  
800 partnership advanced technology microwave sounder for numerical weather prediction and tropical cyclone  
801 applications. *Journal of geophysical research: atmospheres*, 117(D19), <https://doi.org/10.1029/2012JD018144>,  
802 2012.
- 803 Wood, N. B. and T. S. L'Ecuyer: Level 2C Snow Profile Process Description and Interface Control Document,  
804 Product Version P1 R05. NASA JPL CloudSat project document revision 0., 26 pp. Available from  
805 [https://www.cloudsat.cira.colostate.edu/cloudsat-static/info/dl/2c-snow-profile/2C-SNOW-  
806 PROFILE\\_PDICD.P1\\_R05.rev0\\_.pdf](https://www.cloudsat.cira.colostate.edu/cloudsat-static/info/dl/2c-snow-profile/2C-SNOW-PROFILE_PDICD.P1_R05.rev0_.pdf), 2018.
- 807 You, Y., Meng, H., Dong, J., Fan, Y., Ferraro, R. R., Gu, G., & Wang, L.: A Snowfall Detection Algorithm for  
808 ATMS Over Ocean, Sea Ice, and Coast. *IEEE Journal of Selected Topics in Applied Earth Observations and  
809 Remote Sensing*, 15, 1411-1420, DOI:[10.1109/JSTARS.2022.3140768](https://doi.org/10.1109/JSTARS.2022.3140768), 2022.
- 810



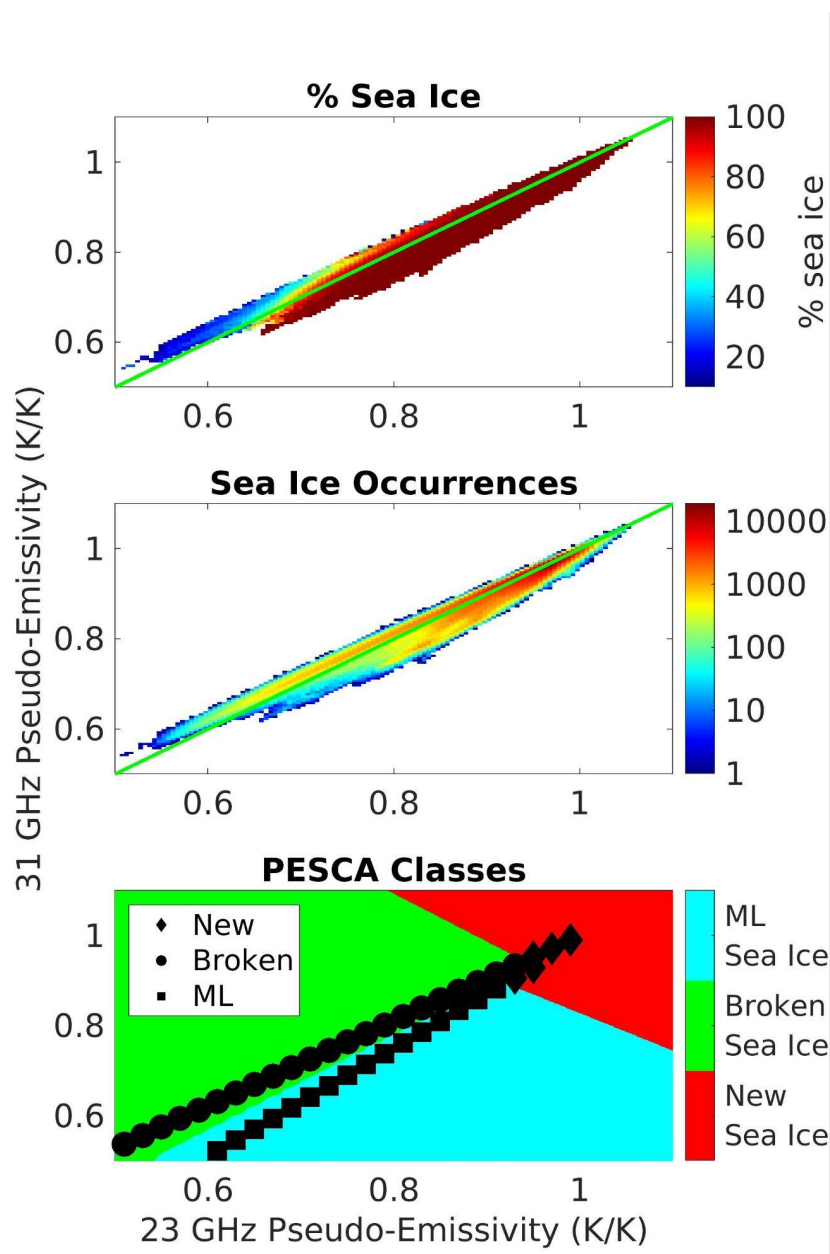
811 Figures



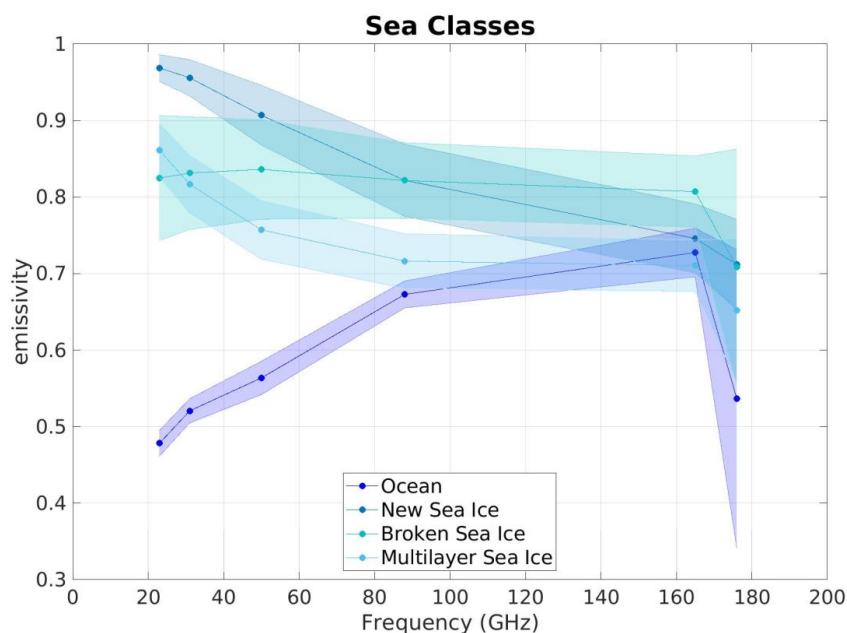
812  
 813 **Figure 1: HANDEL-ATMS workflow diagram (read text for details)**  
 814



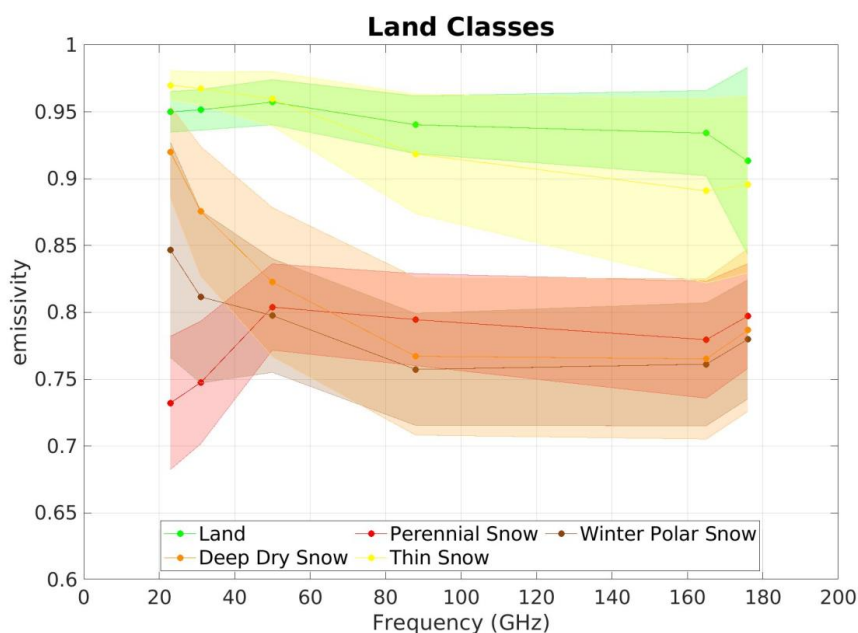
815  
816 **Figure 2: Sea Ice Detection: 23 TB- $T_{2m}$  Plan. The color represents the mean AutoSnow sea ice percentage within each**  
817 **bin (left) and the observation occurrence (right).**



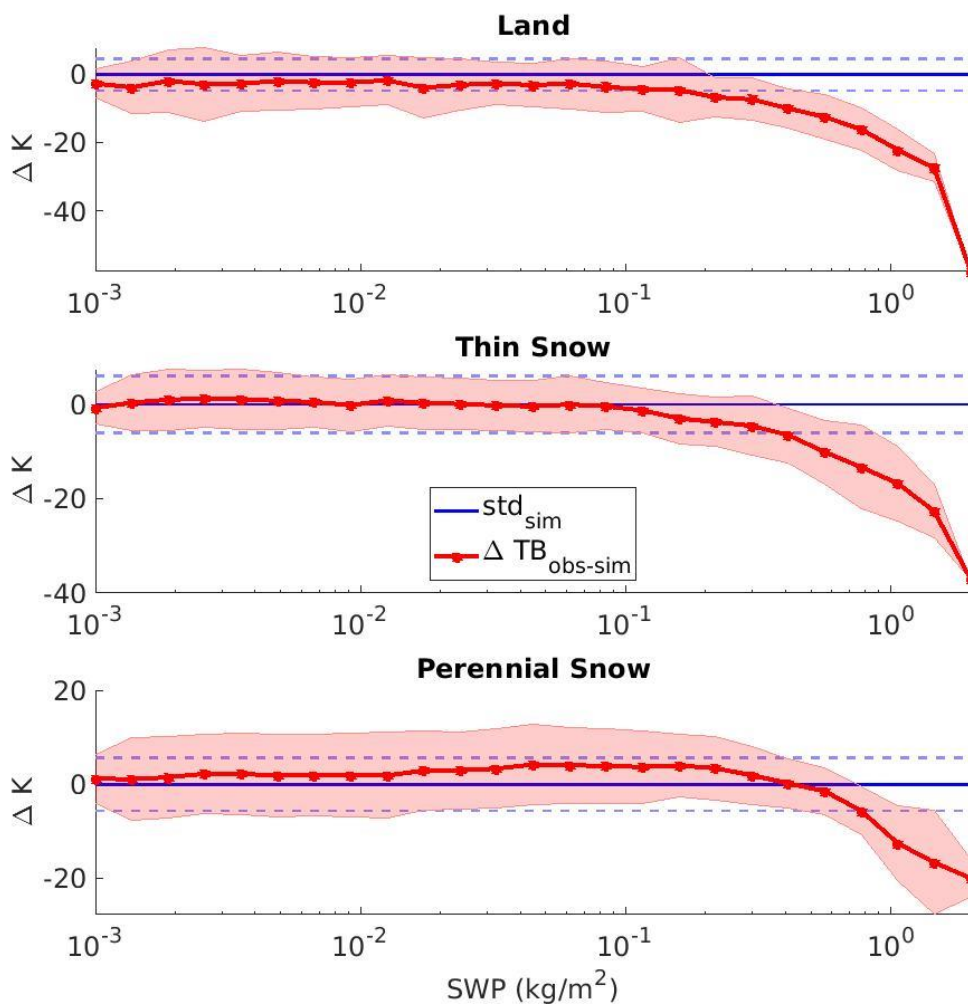
818  
819 **Figure 3: Sea Ice Detection: relationship between 31 GHz Pseudo-Emissivity (y-axis) and 23 GHz Pseudo-Emissivity**  
820 **(x-axis). The color represents the mean AutoSnow sea ice percentage within each bin (top) and the observation**  
821 **occurrence (center) and the PESCA classification with the Nearest Neighbor markers (bottom).**  
822



823  
824 **Figure 4: Emissivity Spectra for PESCA Sea Classes.** The continuous lines represent the mean values of the emissivity  
825 while the shaded areas represent the standard deviation calculated at the ATMS reference frequencies (23.8 GHz, 31.4  
826 GHz, 50.3 GHz, 88.2 GHz, 165.5 GHz, and 183.3 ± 7 GHz) represented by the dots.

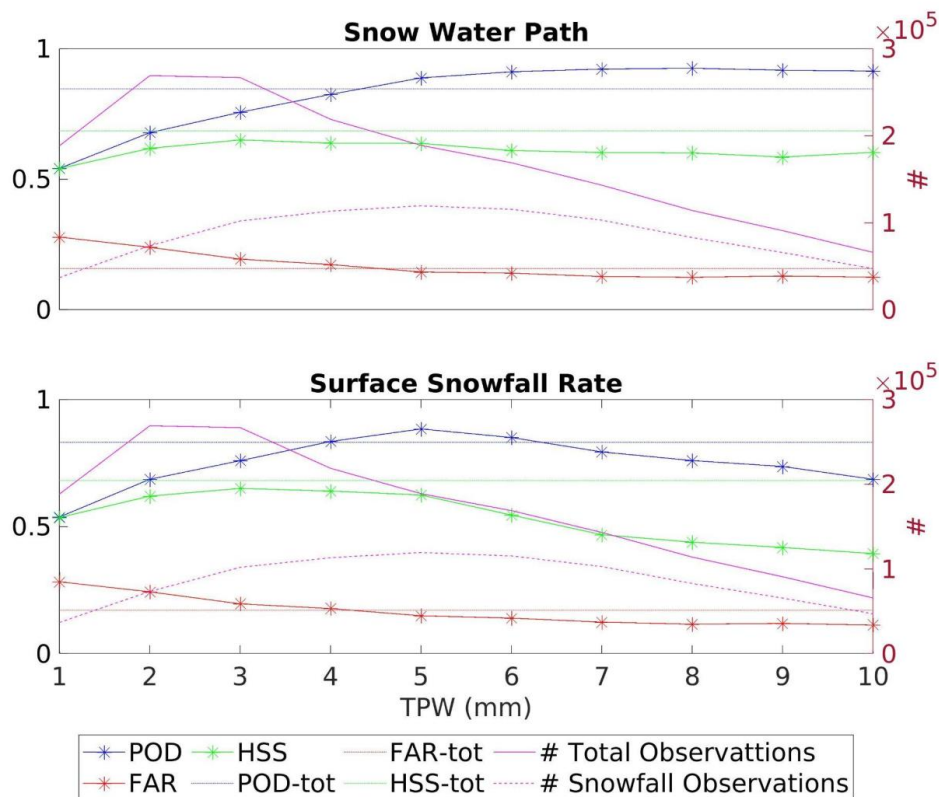


827  
828 **Figure 5: Same as Figure 4 but for PESCA Land Classes.**



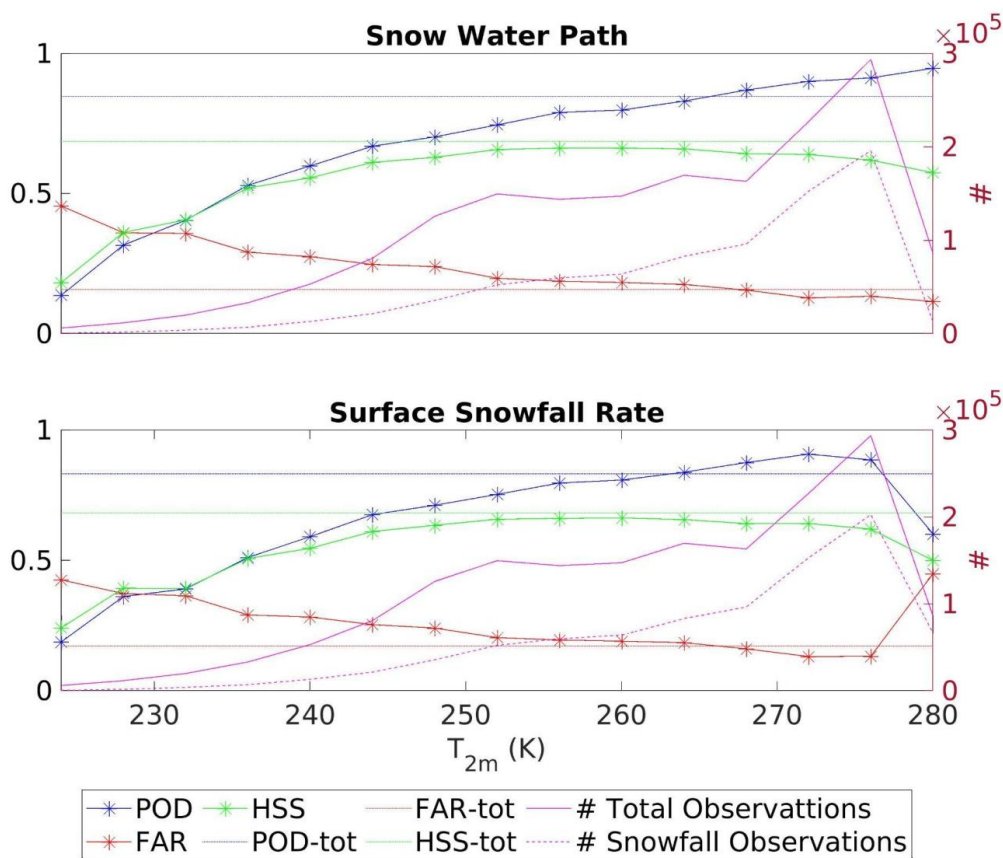
829  
830  
831  
832  
833

Figure 6: 165.5 GHz Snowfall Signature as a function of SWP for three Land surface Classes. The red line and shaded areas represent the mean values and standard deviations of  $\Delta TB_{\text{obs-sim}}$  (i.e., the snowfall signature) while the blue lines are centered on the estimated bias and standard deviation of  $\Delta TB_{\text{obs-sim}}$  in clear sky conditions for the corresponding PESCA surface class.



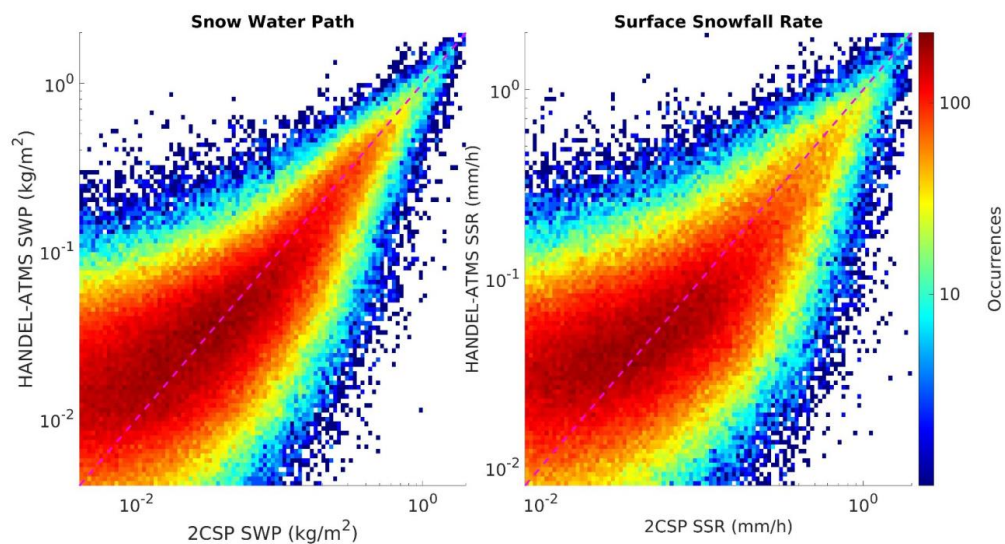
834  
 835  
 836  
 837  
 838

Figure 7 HANDEL-ATMS SWP and SSR Detection Performances for different bins of TPW. The left y-axis reports POD, FAR and HSS vales, while the right y-axis reports the total number and snowfall observations in the dataset. POD-tot, FAR-tot and HSS-tot (dotted lines) represent the statistical scores estimated on the total dataset (values reported in Table 2).

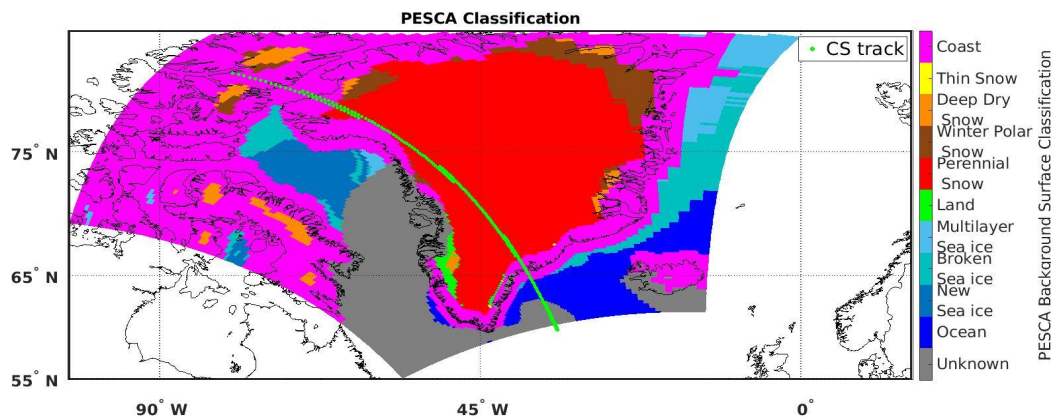


839  
 840  
 841

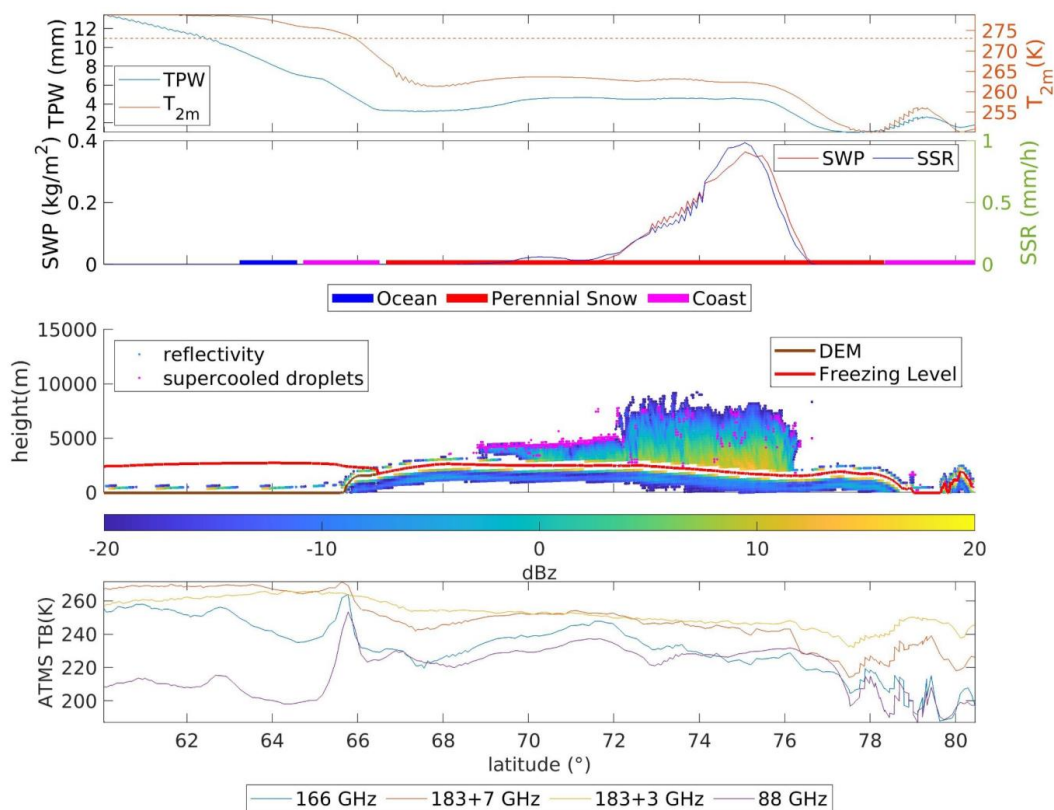
Figure 8: Same as Figure 7 but for  $T_{2m}$  bins.



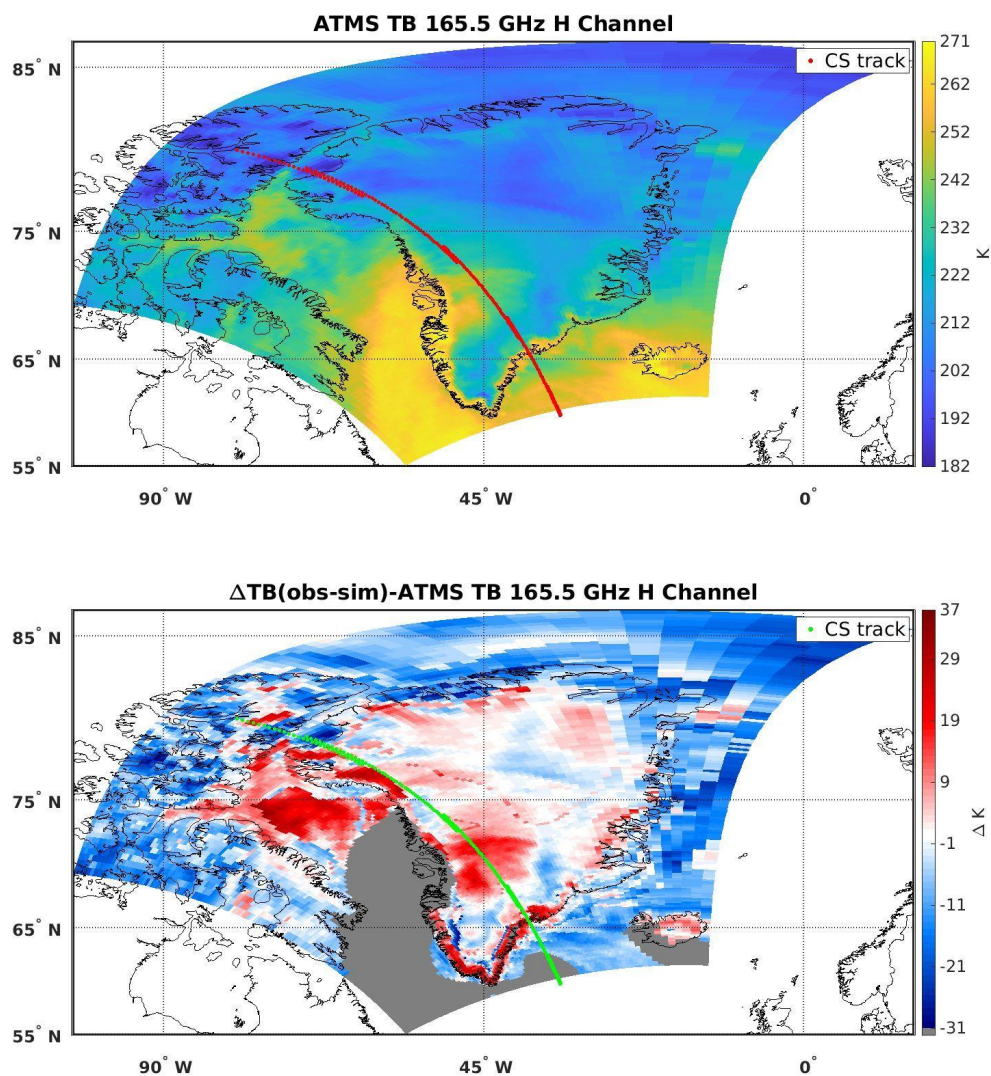
842  
 843 **Figure 9:** 2D Histogram reporting HANDEL-ATMS SWP (left) and SSR (right) estimation and 2CSP. The colorabar  
 844 represents the observation number for each HANDEL-ATMS/2CSP bin.



845  
 846 **Figure 10:** Greenland - 2016/04/24 - PESCA Background Surface Classification.

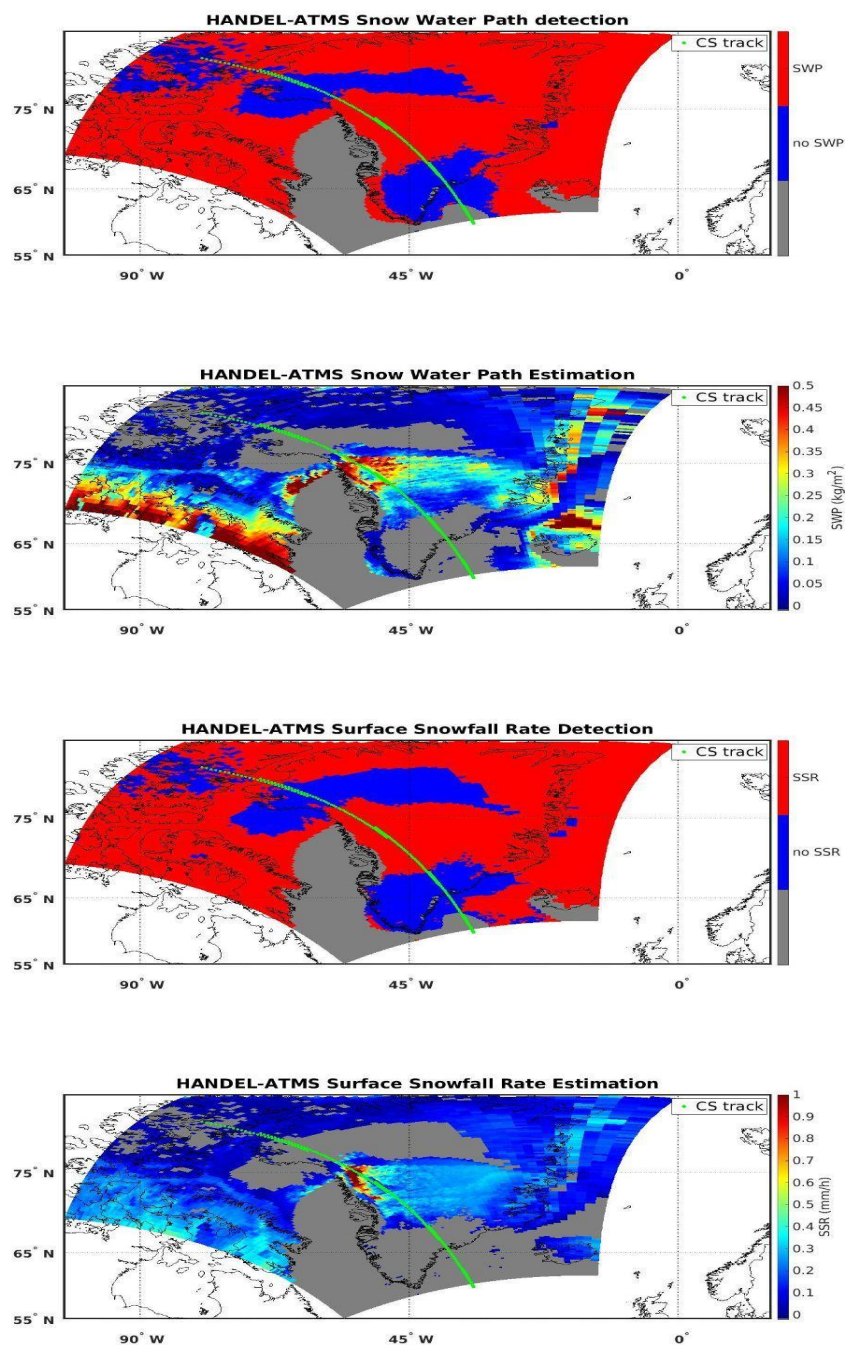


847  
 848 **Figure 11: Greenland - 2016/04/24 - Synopsis along CloudSat Track.** The first panel shows the ECMWF TPW and  $T_{2m}$   
 849 values along the CloudSat track. In the second panel, the 2CSP SWP (left) and the SSR (right) values are reported,  
 850 besides the PESA classification along CloudSat track. In the third panel, the CPR reflectivity (values are reported in  
 851 the colorbar below), the supercooled water droplets detected by DARDAR (magenta points) are shown. Also the Digital  
 852 Elevation Model (brown line) and the ECMWF Freezing Level (red line) along CloudSat track are reported. In the  
 853 bottom panel the observed TBs of the main high-frequency channels (88 GHz, 166 GHz, 183+3 GHz, 183+7 GHz) along  
 854 CloudSat track are shown.  
 855

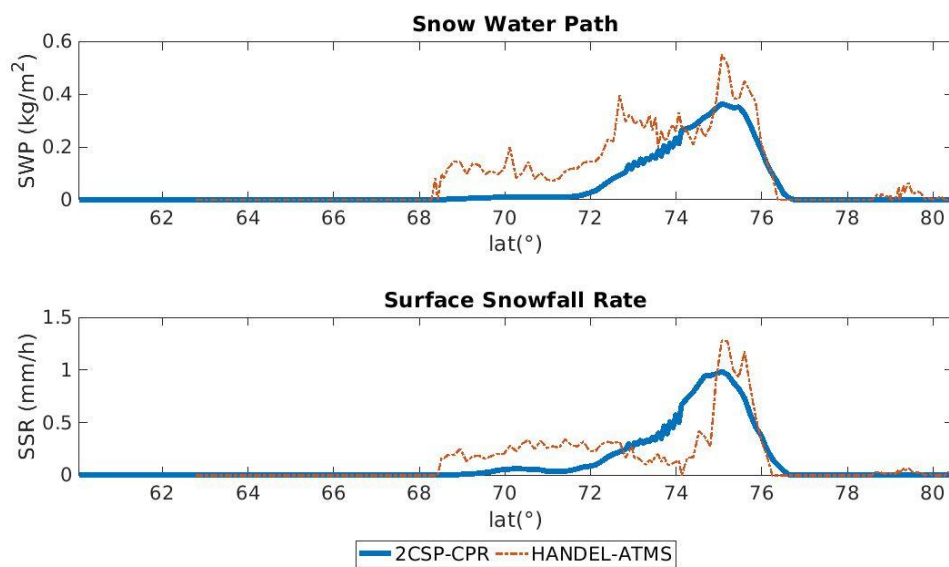


856  
857  
858  
859

Figure 12: Greenland - 2016/04/24 - 165 GHz Channel measured TB ( $T_{B_{obs}}$ ) (top panel) and the deviation of  $T_{B_{obs}}$  from the simulated clear-sky TBs ( $\Delta T_{B_{obs-sim}}$ ) (bottom panel)



860  
861 Figure 13: Greenland - 2016/04/24 - Maps of the HANDEL-ATMS module's output: the SWP detection mask (top  
862 panel), the estimated SWP ( $\text{kg m}^{-2}$ ) (second panel), the SSR detection mask (third panel), the estimated SSR ( $\text{mm h}^{-1}$ )  
863 (bottom panel).



864  
 865 **Figure 14: Greenland - 2016/04/24 - Comparison between CPR 2C-SNOW-PROFILE and HANDEL-ATMS SWP and**  
 866 **SSR estimates along the CloudSat track.**

867  
 868

869 **Tables**

	OCEAN MODULE	LAND MODULE
POD	0.99	0.98
FAR	0.01	0.01
HSS	0.98	0.72

870 **Table 1: PESCA Overall Statistics Scores**

871



Class	n clusters	accuracy	165.5 GHz RMSE (K)	165.5 GHz NRMSE%	Predictor Set
Ocean	2	0.9	3.37	44	$P_{surf} - TPW - T_{2m}$
New Sea Ice	3	0.74	4.52	48	SI - $T_{2m}$ - $P_{surf}$ - ratio - jd - pem <sub>23</sub>
Broken Sea Ice	16	0.56	5.34	41	pem <sub>23</sub> - TPW - SI - $P_{surf}$
Multilayer Sea Ice	9	0.53	4.38	34	pem <sub>31</sub> - SI - TPW - $T_{2m}$ - pem <sub>23</sub> - $P_{surf}$
Land	2	0.87	4.57	52	DEM - jd - TPW
Perennial Snow	8	0.65	5.98	54	pem <sub>23</sub> - jd - SI - pem <sub>31</sub> - lat
Winter Polar Snow	5	0.76	5.87	37	pem <sub>31</sub> - SI - lat - $H_{sol}$ - pem <sub>31</sub> - jd
Deep Dry Snow	15	0.34	6.77	45	SI - pem <sub>31</sub> - ratio
Thin Snow	3	0.78	6.03	39	SI - ratio - lat
Coast	13	0.43	6.80	44	SI - pem <sub>23</sub> - pem <sub>31</sub> - DEM - $T_{2m}$

872 **Table 2: Classification Refinement - Parameters.**

873

Predictor Set	POD	FAR	HSS
$\Delta TB_{obs-sim}$	0.75	0.29	0.48
$TB_{obs}$	0.81	0.18	0.65
$TB_{obs} + environmental\ var$	0.82	0.17	0.68
$TB_{obs} + \Delta TB_{obs-sim}$	0.84	0.16	0.69

874 **Table 3: HANDEL-ATMS SSR Detection Performance: Statistical scores for different Predictor Sets**

875

	POD	FAR	HSS
SWP	0.85	0.15	0.70
SSR	0.84	0.16	0.69

876 **Table 4: HANDEL-ATMS detection Performance - SWP and SSR Detection Modules Statistical Scores**

877

	RMSE	bias	$R^2$
SWP ( $kg\ m^{-2}$ )	0.047	0.001	0.72
SSR ( $mm\ h^{-1}$ )	0.079	0.002	0.61

878 **Table 5: HANDEL-ATMS Estimation Performance - SWP and SSR Estimation Module Error Statistics**

879



880

PESCA Class	SWP		SSR	
	POD	FAR	POD	FAR
Ocean	0.95	0.11	0.91	0.12
New Sea Ice	0.78	0.19	0.79	0.20
Broken Sea Ice	0.83	0.18	0.85	0.19
Multilayer Sea Ice	0.81	0.18	0.81	0.18
Land	0.76	0.16	0.79	0.20
Perennial Snow	0.77	0.21	0.72	0.21
Winter Polar Snow	0.73	0.22	0.74	0.23
Deep Dry Snow	0.83	0.16	0.84	0.17
Thin Snow	0.88	0.16	0.88	0.18
Coast	0.80	0.18	0.80	0.19

881 **Table 6: Comparison between HANDEL-ATMS detection Performances for the Different PESCA surface classes.**  
 882

	POD		FAR	
	SLALOM-CT	HANDEL-ATMS	SLALOM-CT	HANDEL-ATMS
TPW<10 mm T <sub>2m</sub> <280 K (*)	0.82	0.84	0.19	0.16
TPW<5 mm T <sub>2m</sub> <250 K	0.64	0.68	0.28	0.23
TPW<3 mm T <sub>2m</sub> <240 K	0.45	0.54	0.33	0.28

883 **Table 7: Comparison between HANDEL-ATMS and SLALOM-CT detection Performances for Different**  
 884 **Environmental Conditions (\* HANDEL-ATMS working limits).**  
 885